



The Psyche Topography and Geomorphology Investigation

Ralf Jaumann¹  · James F. Bell III² · Carol A. Polanskey³ · Carol A. Raymond³ · Erik Aspaugh⁴ · David Bercovici⁵ · Bruce R. Bills³ · Richard Binzel⁶ · William Bottke⁷ · John M. Christoph² · Simone Marchi⁷ · Alicia Neesemann¹ · Katharina Otto⁸ · Ryan S. Park³ · Frank Preusker⁸ · Thomas Roatsch⁸ · David A. Williams² · Mark A. Wieczorek⁹ · Maria T. Zuber⁶

Received: 7 June 2021 / Accepted: 15 February 2022 / Published online: 8 March 2022
© The Author(s) 2022, corrected publication 2022

Abstract

Detailed mapping of topography is crucial for the understanding of processes shaping the surfaces of planetary bodies. In particular, stereoscopic imagery makes a major contribution to topographic mapping and especially supports the geologic characterization of planetary surfaces. Image data provide the basis for extensive studies of the surface structure and morphology on local, regional and global scales using photogeologic information from images, the topographic information from stereo-derived digital terrain models and co-registered spectral terrain information from color images. The objective of the Psyche topography and geomorphology investigation is to derive the detailed shape of (16) Psyche to generate orthorectified image mosaics, which are needed to study the asteroids' landforms, interior structure, and the processes that have modified the surface over geologic time. In this paper we describe our approaches for producing shape models, and our plans for acquiring requested image data to quantify the expected accuracy of the results. Multi-angle images obtained by Psyche's camera will be used to create topographic models with about 15 m/pixel horizontal resolution and better than 10 m height accuracy on a global scale. This is slightly better as global imaging obtained during the Dawn mission, however, both missions yield resolutions of a few m/pixel locally. Two different techniques, stereophotogrammetry and stereophotoclinometry, are used to model the shape; these models will be merged with the gravity fields obtained by the Psyche spacecraft to produce geodetically controlled topographic models. The resulting digital topography models, together with the gravity data, will reveal the tectonic, volcanic, impact, and gradational history of Psyche, and enable co-registration of data sets to determine Psyche's geologic history.

Keywords Psyche · Asteroide topograph · Asteroide geology · Mapping strategy

1 Introduction/Background

The objectives of the Psyche mission are to investigate the processes and conditions that formed the asteroid Psyche that also affected its subsequent geologic evolution. The shape

The NASA Psyche Mission: Science Instruments and Investigations
Edited by James F. Bell III, Carol Polanskey, and Lindy Elkins-Tanton

Extended author information available on the last page of the article

and detailed topography of asteroid Psyche may have recorded much of its history, including differentiation, possible magmatism, convective motions and bombardment history, as well as the nature of surface alteration by gradational (weathering, erosion and depositional) processes.

Asteroid Psyche's high density of $3.88 \pm 0.25 \text{ g/cm}^3$ (Sitala and Granvik 2021) suggests an unexplored surface mineralogy partly composed of metallic compounds with specific reaction to geological processes (for a review, see Elkins-Tanton et al. 2020). The reconstruction of the shape, along with the gravity fields, will allow inferences on the internal structure, while basins, crater shapes, lineaments, ridges, graben, and volcanic constructs will provide a framework for interpreting the images and spectral data to determine the geologic history of Psyche. By exploring the formation and evolution of Psyche, we glean insights into the nature of other objects in the asteroid belt and possibly the interiors of differentiated objects that coalesced to form the terrestrial planets.

Image data provide the basis for extensive studies of the surface structure and morphology on local, regional, and global scales. This is accomplished by extracting geomorphologic information from images, topographic information as derived from digital terrain models (DTMs), and spectral information from color images (i.e. Jaumann et al. 2012). Knowledge of the magnitudes as well as the directions of slopes is needed to understand such quantities as the depths of craters and depressions, the viscous response of materials to stress, the heights of mountains and thus the volumes of geological features. Direct topographical measurements are also needed to determine whether more than one phase of deformation (Fossen et al. 2019) is present and the degree of erosion of the surface from meteoritic and thermal processes (i.e. Delbo et al. 2014). Additionally, for asteroids like Psyche with a surface gravity less than 1% that of the Earth, and much lower interior stresses, these topographic expressions are likely to be more global in scale and can constrain the asteroid's internal structure, formation and geology. Deeply excavating craters can thus probe the global properties (e.g. Jutzi et al. 2013), as can global faults (Buczowski et al. 2012) and antipodal units.

Determining physical surface properties also provides geologic context. Identification of geologic units in terms of morphology, structure, age and compositional heterogeneities depends on local relief and the direction of slopes. Relationships of different geologic units define stratigraphic sequences, which are used to model the processes that formed specific surface features. Topographic measurements are thus crucial for these investigations and are also used to refine the geodetic control network needed for gravimetric investigations (Raymond et al. 2011; Park et al. 2016). A comprehensive evaluation of the data from the Psyche Multispectral Imagers, based on the image-derived topographic image base maps, will enable combined structural/compositional investigations using camera and spectrometers.

Like Dawn, Psyche is principally a systematic mapping mission to a previously unexplored object. Thus, there are no requirements for targeted observations; nor can the shape and gravity field be sufficiently characterized until arrival. As demonstrated by Dawn close-orbiting experience (Rayman and Mase 2014; Parcher and Whiffen 2011; and Kennedy et al. 2013) a large, unmapped asteroid requires a recursive approach in which science observations in one orbit enable refinement of the gravity field and shape model so as to plan the transfer to the next lower orbit. Psyche will execute a series of four progressively lower circular orbits and spend 20 months in orbit observing Psyche simultaneously with all science instruments. Topographic maps are produced using the stereo photogrammetry (SPG) and stereo photoclinometry (SPC) techniques mainly developed by the Dawn mission (Raymond et al. 2011; Polansky et al. 2012; Jaumann et al. 2012; Preusker et al. 2016).

2 Current Geomorphological Knowledge

2.1 Landforms

Asteroid Psyche is suggested to have at least one large impact crater near its south pole, similar to that found on (4) Vesta (Shepard et al. 2017; Viikinkoski et al. 2018). In addition, the shape of Psyche as modelled by Ferrais et al. (2020) indicate deviations from an ellipsoid, interpreted as three large depressions along its equator. According to the model of Ferrais et al. (2020) the flatness and density of Psyche are compatible with a formation at hydrostatic equilibrium with a shorter rotation period that may have later slowed down by impact events. With its low gravity, the interior stresses inside of Psyche are much less than 1 kbar, comparable the stress conditions found a few 100 meters below the surface of the Earth; a solid Psyche can maintain a substantial disequilibrium shape attributed to its formation.

Mostly due to the two large south polar impacts Veneneia and Rheasilvia, the surface of Vesta exhibits extended undulated landforms (Thomas et al. 1997; Jaumann et al. 2012; Schenk et al. 2012). The ratio of the amplitude of surface relief to the radius of Vesta is $\sim 15\%$, meaning that topography locally adds or subtracts 1/5th of the body's average radius! Compared to a $\sim 1\%$ ratio for the Moon and Mars steep slopes $> 10^\circ$ up to 30° are much more common on Vesta. And like Vesta, Psyche has a rapid rotation (4.1 hr), which means that mega-crater formation happens in the presence of Coriolis forces that could dramatically influence the final topography (Jutzi and Asphaug 2011; Otto et al. 2016). Also Pallas records a violent collisional history, with numerous craters larger than 30 km in diameter populating its surface and two large impact basins which might consider Pallas a preview for Psyche although the surface strength of Psyche is most likely much higher than Pallas (Marsset et al. 2020).

Considering the expected large impact craters on Psyche, the ratio of the amplitude of surface relief to radius is likely to be at least 10% also resulting in steep slopes, depending upon how much silicate regolith is contained on the surface. Steep slopes will also encourage gravitationally driven mass wasting, which is a significant landscape forming and erosive processes on Vesta (Otto et al. 2013; Krohn et al. 2014). Next to granular landslides and impact ejecta related flow-like features, Vesta also exhibits pervasive slumping of more competent material along the crater rim of the large impact basin Rheasilvia. Given the potentially high strength of Psyche's crust and the steep slopes, large scale mass-wasting including slumping can therefore be expected. Therefore, Psyche is expected to exhibit Vesta like asymmetric craters formed by impacts on steep slopes, which results in a sharp upslope crater rim, and a muted downslope crater rim because of preferential accumulation of ejecta downslope (Jaumann et al. 2012; Krohn et al. 2014). However, the shapes of craters on Psyche may differ significantly from what we know from Vesta due to a high content of metal and differing impact velocities (Libourel et al. 2019; Marchi et al. 2019). The dependence of crater collapse on target strength has already been shown for silicate Vesta and ice-rich Ceres (Schenk et al. 2021). Larger craters on Psyche are also expected to undergo gravity-driven collapse at the end of the excavation phase but on high strength metallic bodies, collapse might be suppressed (Elkins-Tanton et al. 2020). In addition, the distribution of silicates on Psyche will therefore result in different stratifications of the near-surface that are exposed by impact cratering (Elkins-Tanton et al. 2020). Extensional features caused by the pressure response of large impacts could be produced, such as the Divalia and Saturnalia Fossae observed on Vesta (Jaumann et al. 2012; Buczkowski et al. 2012). In this context steep hills and elongated depressions would provide an environment for mass wasting and collapse. Psyche's higher density compared to Vesta, and thus its metal fraction, could yield

crater morphologies with steeper slopes. More competent material could result in ejecta dominated by large blocks and less sorting of regolith particles. From more details about putative impact structure on Psyche see Marchi et al. (2022) this issue.

Although impact craters are expected to dominate Psyche's morphology, a large impact basin and/or large impact crater could cause global features such as ancient compressional blocks resulting in mountainous complexes like Vestalia Terra on Vesta, possibly including dike-like features (Buczowski et al. 2014). Johnson et al. (2020) describes a process where core material intrudes into the overlying rocky mantle or possibly even erupts onto the surface as ferrovulcanism eruptions that may produce volcanic landforms on Psyche.

2.2 Surface Alteration

The evidence of a thick regolith layer on Vesta (Jaumann et al. 2012; Denevi et al. 2016), the Moon, and all planetary airless bodies with a solid surface prove the effectiveness of weathering by solar wind, meteoroid, asteroid, and cometary bombardment. Primary planetary crusts are covered by globally and regionally distributed ejecta. Craters are eroded by bombardment and covered by subsequent ejecta of larger impacts resulting in impact-induced resurfacing by the formation of multiple regolith layers. Steep slopes and failure support mass wasting and scarp formation yielding additional resurfacing by landslides.

However, regolith on Psyche will be subject to a possible metallic component mixed into silicate particles. In addition to the metallic component originating from Psyche's bulk composition, metal-bearing silicate, sulfide, and oxide minerals are chemically reduced by space weathering processes including solar wind ion irradiation (Pieters et al. 2000) and micrometeoroid impact (Sasaki et al. 2001), forming metallic iron particles at a variety of length scales up to ~ 10 microns (Noguchi et al. 2014; Matsumoto et al. 2020). Thus, components of different density, size and sorting are predicted to dominate the regolith resulting in complex block-dominated mass wasting features (Kleinhans et al. 2011). The angle of repose of freely moving grains is higher on smaller bodies: lesser gravity allows grains to pile at higher angles before slipping downslope. Ermakov et al. (2019) finds that the angle of repose on Vesta and Ceres is around 34° , while on the Moon and Mars it is closer to 30° , and on the Earth lower still. This means that where regolith is formed on asteroids, we can predict it to pile into steeper slopes assuming the same regolith particle shapes and sizes. Thus, with Psyche's even lower gravity, its angle of repose may be higher than that of Vesta.

Importantly, it is not clear if metal forms a regolith at all. Regolith on Psyche may be mainly rocky material. If a metallic regolith exists, grains might be less regular, and therefore more interlocking capable of forming even steeper slopes? Or would it be mainly smooth tektites formed by impacts into metal, and therefore slipperier and forming shallower slopes? If metal and silicate particles are mixed the regolith become more complex with respect to its physical properties. Haack et al. (2020) mixed spherical and angular particles and measured the tensile strength of different mixing ratios (proxy for the steepness of the slopes). They found that the strength of spherical and angular particle mixtures is dominated by the stronger component (angular particles) and that it varies up to two orders of magnitude between purely spherical and purely angular particles. It is also possible that larger agglutinates will form by impact gluing together silicate particles by molten metal increasing the grain size of the regolith. The grain sizes of regolith on asteroids can be predicted including thermal, polarimetric, photometric, and spectroscopic data (e.g. Hicks et al. 2014; Hiroi et al. 1994). Capria et al. (2014) used VIR thermal data to estimate the thermal inertia of Vesta's surface, and thereby estimate the surface particle size range. They conclude that Vesta has a regolith with grain sizes and properties similar to that of the Moon, with a

size range from microscopic to multi-meter blocks. Thermal inertia estimates of Psyche are 133 or $114 \text{ J m}^{-2} \text{ s}^{-0.5} \text{ K}^{-1}$ (Matter et al. 2013), which is among the highest thermal inertia values measured for an asteroid of this size, supporting evidence of a metal-rich surface for Psyche. However, a study by Landsman et al. (2018) reported thermal inertia values that were representative of a silicate regolith.

Considering a metallic substrate on Psyche will additionally cause fracture from impact shock resulting in large-scale displaced bedrock units and metallic blocks in the meters to tens-of-meters range. However, it is unclear whether blocks in this size range remain angular and intact or the heat transfer will partially melt the metals forming breccias? It is also unclear what the smallest possible block originating from impact shock without melting may be in metal, whether meter-scale boulders, tens-of-cm-scale cobbles, cm-scale gravel, or smaller. Investigations into shock darkening e.g. Moreau et al. (2019) have found that even mm-scale differences in shock impedance, as in a regolith with mixed metallic and non-metallic particles, are enough to drive significant local heterogeneity in shock pressure and temperature, resulting in partial melting of the metallic fraction. Whether similar effects occur at cm-scales or larger is unclear.

Impact experiments on metal yield a variety of metal ejecta fragments (Marchi et al. 2019), with preliminary characterization indicating a wide range of alteration textures from fully-melted microtektites to shock-fractured shards preserving pre-impact microstructure (Christoph et al. 2021). Therefore mm- and cm-sized metal impact melted spherules and impact shards could interact with silicate particles. Shaking from impacts and sliding may sort this material. Impact experiments on metal yield a variety of metal microtektites (Marchi et al. 2019). Therefore mm- and cm-sized metal tektite spheres may interact with silicate particles. Shaking from impacts and sliding may sort this material. The interactions of metal and silicate particles, thus, are possibly complex and difficult to predict. Variations in surface roughness, mixtures of minerals or meteorite types, and optical properties like phase angle and polarization of collected asteroid spectral data (i.e., Britt and Pieters 1988; Cloutis et al. 1990a,b; Lupishko and Belskaya 1989; De Sanctis et al. 2012, 2013; Stephan et al. 2014; Figeri et al. 2015) also expect Psyche having a surface that is dominated by relatively fine-grained (20–50 μm in size) iron-nickel metal, but with a significant component of low-Fe, low-Ca orthopyroxene. The brittle-ductile transition for metal will also affect the outcome of cratering on Psyche because the strength of the metal increases for lower temperatures (Marchi et al. 2020, 2022 this issue).

3 Topography of Asteroids

Asteroids can be highly irregular planetary bodies, with some showing an order of magnitude higher topography to radius ratio than planets or moons. Detailed mapping of topography is central to understanding of processes shaping surfaces. Topography is fundamental for studying their surfaces and interiors, yielding information on landforms, slopes and local surface properties such as roughness as well as internal density variations. The shape of Psyche is essential to properly invert gravity data of asteroids and derive a robust modeled interior structure. Detailed impact crater shapes, slopes, as well as the form of any surface feature provides fundamental morphometric constraints on geological processes that have operated on surfaces (Jaumann et al. 2012).

On asteroids, the shape of craters, possible surface deflection by mass loads, and mass wasting and regolith movement and front shapes, provide constraints on rheology over time and depth. Topography is obtained by a combined solution using camera views at various

angles and multiple views of each surface element. Camera-derived surface heights enable the development of regional grids for quantitative studies of surface processes. Stereo information, combined with precise gravity field models, also provides a geodetic control grid at sufficient scale, in which to co-locate other data types at absolute positions on the bodies. Both the imaging and the gravity datasets can provide information needed to resolve internal heterogeneity. At shorter scales and at lowest altitudes the thickness of the crust can be deduced. Geomorphologic studies require slope information at a few percent at the scale of the smallest resolved craters. Optical observation contributes to the topography objective via stereo imaging, from which digital terrain models at high spatial resolution (on the order of the camera pixel size) are derived (i.e. Jaumann et al. 2007; Raymond et al. 2011; Preusker et al. 2012; Gwinner et al. 2016). These digital terrain models provide fundamental insight into geological processes and help constrain studies of the formation and evolution of the crust.

The combination of gravity, topography, and surface composition data is key to modeling the entire structure and composition of a body. Image data provide the basis for extensive studies of the surface structure and morphology on local, regional, and global scales using the photogeological information, the topographic information from the derived digital terrain model, spectral information from color images, and spectral reflectance data. Knowledge of the magnitudes as well as the directions of slopes is needed to understand such quantities as the viscosities of flow features and lavas, and hence their possible composition, the volumes of constructs and flows, the depths of craters/depressions, and the heights of mountains.

Direct topographical measurements are also needed to determine whether polyphase deformation (i.e. Fossen et al. 2019) is present and the degree of erosion of the surface. Identification of geologic units in terms of structure, age and compositional heterogeneities depends on local relief and the direction of slopes. Relationships of different geologic units define stratigraphic sequences, which are used to model the processes that formed specific surfaces. Topographic measurements are crucial for these investigations and are also used to refine the geodetic control network needed for gravimetric investigations. Topography of small bodies improved the science output of the orbiting missions Dawn, Rosetta, Hayabusa 2 and Osiris-REx yielding detailed insight into the shape and structure of Vesta, Ceres, Ryugu and Bennu (i.e. Jaumann et al. 2012; Preusker et al. 2012, 2016; Fu et al. 2017; Watanabe et al. 2019; Sugita et al. 2019; Lauretta et al. 2019) and supported landing and sampling (i.e. Preusker et al. 2019; Scholten et al. 2019; Park et al. 2019).

4 Methodology

Imaging data have been used to generate topography data set in planetary exploration. Two approaches will be used to quantify the topography of the surface of Psyche; these are stereo-photogrammetry (SPG) and stereo-photoclinometry (SPC), which also uses a shape-from-shading approach. Both techniques are applied to multiple optically observed images of the same region (Jaumann et al. 2007; Gaskell et al. 2008; Raymond et al. 2011). *Photogrammetry*, the geometrical analysis of stereo pairs of optical images, has provided much of our knowledge about the quantitative topography of Earth and other planets. *Photoclinometry* is an alternative approach that can be applied to unpaired images and can achieve single-pixel resolution, because it is based on interpreting brightness (shading) variations in slopes rather than measuring geometrical parallaxes. It is more model-dependent and requires additional data for scaling and absolute referencing. The Psyche team will also use a refined

photoclinometric technique (photoclinometry by deformation, or PCD) that can iteratively solve for both the slopes and albedo variations, thus reducing the model-dependence in the photoclinometric solution (Raymond et al. 2011).

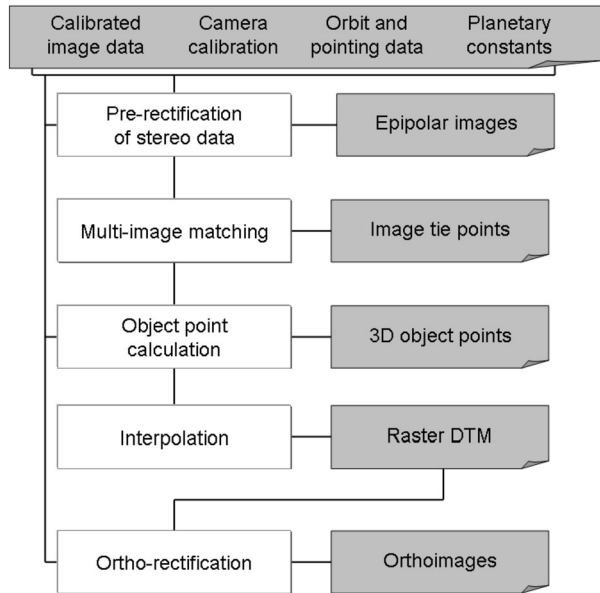
4.1 Stereophotogrammetric Mapping (SPG)

Photogrammetric processing will derive three-dimensional models of Psyche's surfaces and ortho-rectified images (orthoimages). The raw camera data received from the spacecraft are sorted, adjusted by acquisition times, decompressed and radiometrically calibrated. Camera ancillary data (geometric distortion model), as well as other external geometric information such as orbit and attitude data. A variety of panchromatic and color three-dimensional products can be achieved by means of stereo-photogrammetric processing, i.e., Digital Terrain Models (DTMs), multi-spectral orthoimages, image mosaics, and finally various types of 3D-visualizations and cartographic products. DTMs are the main high-level products that serve as a precise description of Psyche's topography for science and for ortho-rectification of image data at high spatial resolution. Considerable experience related to the photogrammetric processing of planetary data has been gained over more than 15 years from various planetary missions (e.g., Jaumann et al. 2007; Scholten et al. 2009; Raymond et al. 2011; Jaumann et al. 2012; Preusker et al. 2015, 2016; Gwinner et al. 2016). The stereophotogrammetric derivation of a DTM relies on area-based multi-image matching of two or more images. From the combination of the resulting tie point coordinates, combined with the interior camera geometry, and information of the orbit position and pointing, a 3-dimensional forward ray intersection yields an irregular grid of object points, which is used to interpolate a final raster DTM. Generally, the quality of DTMs and orthoimages strongly depends on the accuracy of the orientation data such as the well calibrated interior camera geometry, the reconstructed position and attitude spacecraft pointing data derived from radio tracking and optical navigation and combined with results from photogrammetric block adjustment information.

The photogrammetric DTM generation process chain (Fig. 1) is embedded in an iterative procedure. A coarse-to-fine iteration includes photogrammetric block adjustment in order to improve the initial spacecraft/position, pointing direction, and the alignment of the camera to the spacecraft. Subsequently, intermediate DTMs are calculated and serve as input for pre-rectification. Once iterations of all global stereo image dataset have yielded full-resolution tie point coordinates the final orientation is derived by an overall photogrammetric adjustment of the entire global block yielding the final stereo DTM interpolation.

Stereo data are pre-rectified to a constant pixel scale in common geometry based on preliminary orbit and pointing information. With remaining parallaxes, the deviation of the *a priori* topography assumption to the true shape of the body can be estimated to enable linking the pre-rectification geometry to the raw image geometry. Applying a multi-image matching technique to pre-rectified image allow to derive conjugate points in each of the stereo observations. The algorithm uses area-based correlations in image pyramids to derive approximate values for the image coordinates, refine sub-pixel accuracy by least-squares matching (Gwinner et al. 2009). After multi-image matching, the derived image coordinates of all stereo observations are transformed back to raw radiometrically corrected data geometry, using the history files generated during the pre-rectification. The accuracy of this back-transformation is better than one tenth of a pixel (Scholten et al. 2005). Lines of sight as defined by the image coordinate pair for each stereo observation, the geometric calibration, and the orientation data, with least-squares adjustment are used for forward ray intersection,

Fig. 1 Processing line for DTM generation from stereo data (Raymond et al. 2011)



resulting in object points defined in body-fixed Cartesian coordinates. Multi-stereo capability enables minimization of the influence of occasional gross matching errors, which cannot be avoided by simple two-image matching.

Object points are transformed from body-fixed Cartesian coordinates to geographic latitude/longitude/height values based on a three-dimensional reference system. The geographic latitude/longitude coordinates of all object points from all stereo image sets are transformed to standard map projections (equidistant projection for equatorial regions up to $\pm 85^\circ$, stereographic projection for polar regions). Object points located within a DTM pixel are averaged and can optionally be combined by different filtering techniques with those within a chosen neighborhood (Gwinner et al. 2009). For regions that lack any object point information, a final gap-filling algorithm using DTM pyramids with reduced resolution can be applied.

Ortho-rectification uses ray-tracing of the regular pixel positions of the input radiometrically-corrected pixel matrix with the DTM based on interior camera calibration and exterior orientation data (Scholten et al. 2005). A 3-D intersection point with the DTM is derived for each grid point and transformed to the map projection of the output orthoimage with the same standard projections as for the DTM. For each pixel within a mesh of these transformed grid points, an indirect resampling based on different selectable interpolation methods is performed within the radiometrically corrected input matrix in order to derive the final orthoimage grey value. Finally, ortho-rectified color and panchromatic channels, if rectified to the same map projection and pixel scale, fit to each other with the accuracy provided by the DTM and the applied orientation data and can be superimposed as co-registered multi-spectral/multi-phase data sets (Scholten et al. 2005). Ortho-rectified images of different orbits are combined to one common image mosaic using image information in overlapping areas for producing seamless transition from image to image by weighted averaging of overlapping image parts. The geometric relationship between the images to be mosaicked is considered to be fixed and is defined by each image's label information comprising nominal map projection parameters, scale, and the offset of its upper left pixel with respect to the projection center. Statistics of the density of object points (Gwinner et al. 2009), which might

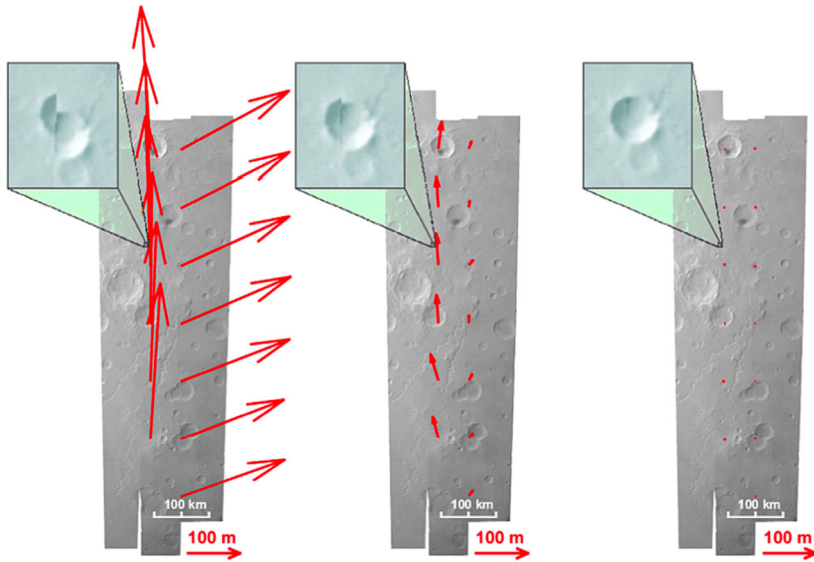


Fig. 2 Example of displacements (red arrows). Identical points are identified in overlapping blocks of Mars Express HRSC images and corrected by bundle block adjustment (Gwinner et al. 2016)

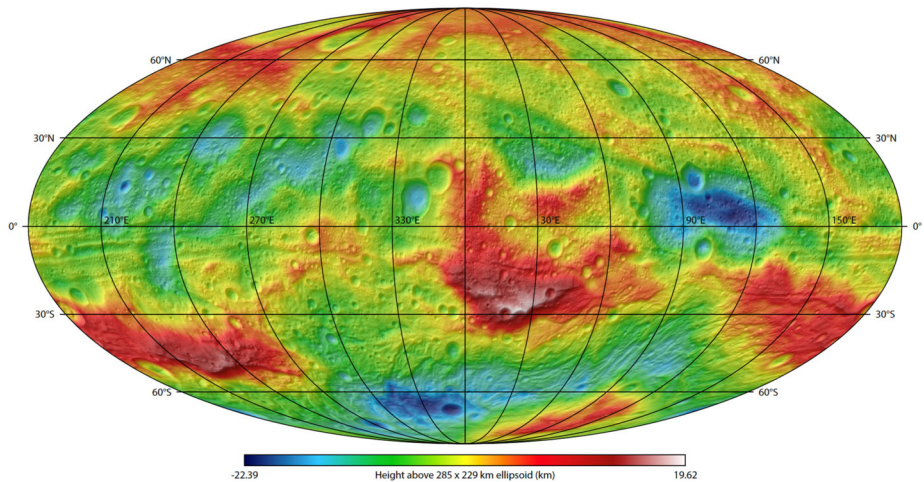


Fig. 3 HAMO-based SPG-derived global topography of Vesta (e.g. Jaumann et al. 2012; Preusker et al. 2012, 2016) superposed on a hill shade model derived thereof. The map is in equal area Mollweide projection in the Claudia Double Prime reference system for Vesta (Li 2012)

be affected by compression effects, variable local texture and varying illumination conditions, will allow a quality assessment of the stereo data processing accuracy. Displacements identified in overlapping images can be corrected by bundle block adjustment (Gwinner et al. 2016) (Fig. 2).

Figures 3 and 4 show final DTM products resulting from stereo data of the Dawn and Mars Express missions.

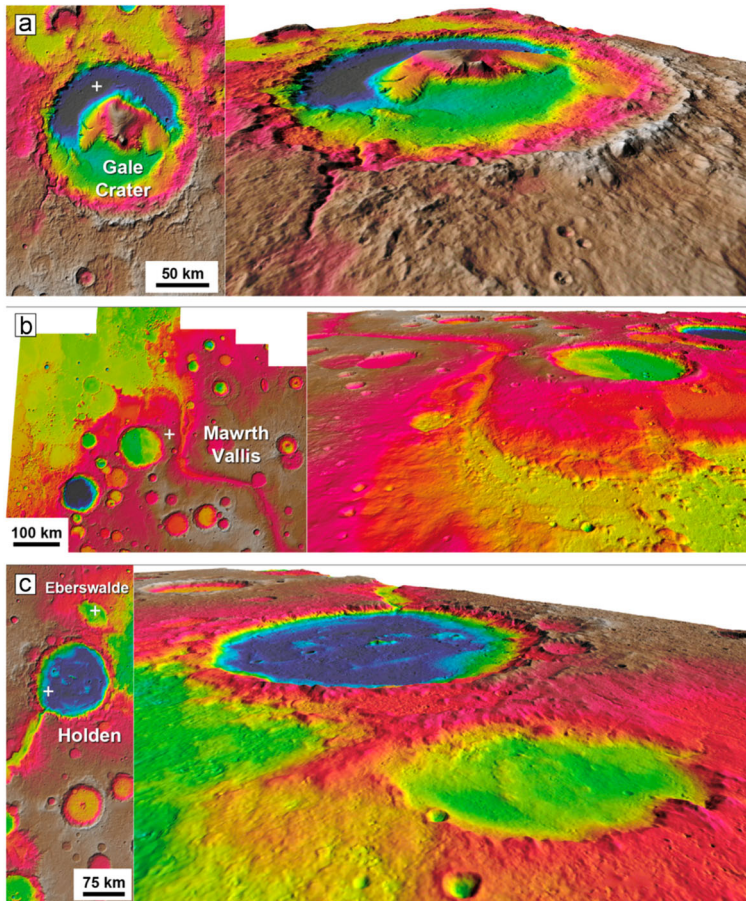


Fig. 4 Examples of final DTM products. Mars Express HRSC multi-orbit DTMs of the final four candidate landing sites of the Curiosity (white crosses centers of proposed ellipses). On the left plan views (norths up); right-side perspective views; color-code elevations (red = high, blue = low). (a) Gale crater; (b) Mawrth Vallis; (c) Holden and Eberswalde craters (Gwinner et al. 2016)

4.2 Stereophotoclinometric Mapping (SPC)

Stereophotoclinometry uses orthorectified projections of many images of a surface patch, observed under differing illumination conditions, to construct a landmark template called a maplet (Raymond et al. 2011; Park et al. 2019). The slope and albedo at each pixel of a maplet is determined by least square minimizing the brightness residuals between the images and illuminated maplet via least square estimation. The slopes are then integrated to produce a digital terrain map (DTM). Figure 5 shows the topo/albedo maplet constructed from 62 NEAR images of Eros, re-illuminated and compared with projected image data. The maplets display the major features of the images and reproduce the brightness variations well.

A maplet identified in a large number of images allows determination of its surface location very precisely, by averaging down spacecraft position errors and camera pointing uncertainties, while a large number of maplets in a single image allow refining spacecraft

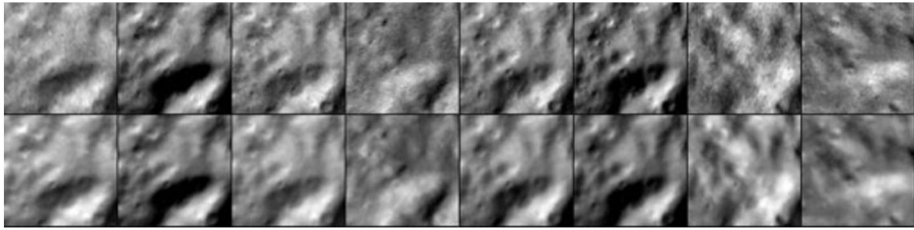


Fig. 5 Illuminated maplet (bottom row) and projected image data (top row) of Dawn stereoscopic data (from Raymond et al. 2011)

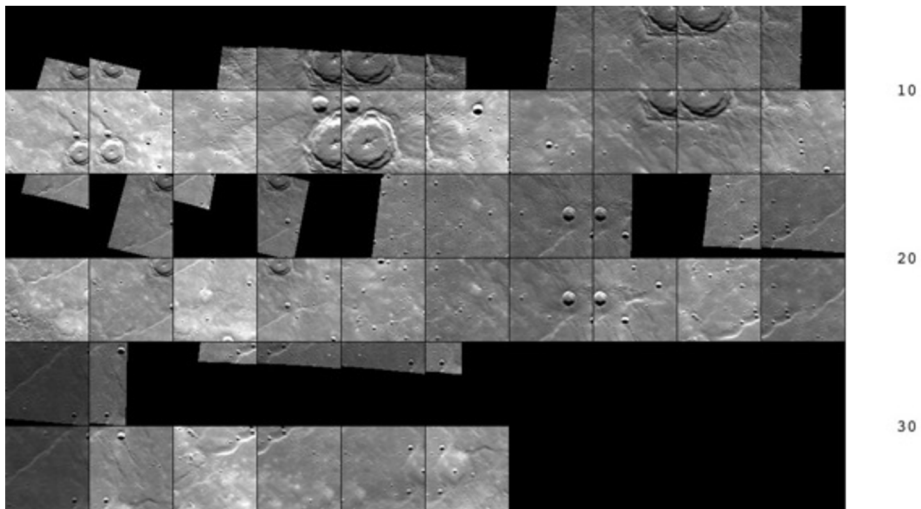


Fig. 6 Auto registration of projected MDIS (MESSENGER) data. Notice that the maplet surface does not have to be completely within an image to be usable (from Raymond et al. 2011)

position and camera pointing estimates. Figure 5 shows an example from an auto registration that solves for the spacecraft state of the MESSENGER mission with the ensemble of existing maplets.

A maplet ensemble is more powerful than a collection of single maplets. Overlapping maplets provide a three-dimensional constraint between the body-fixed locations of their centers. Finally, if the ensemble tiles the entire body, then they can be combined to produce a global topography model (GTM).

An initial set of maplets will be constructed from the first images. As Psyche rotates, a surface feature is seen at varying local sun elevations, allowing to construct the topography from the changing illumination. Correlation of re-illuminated maplet images with the original allow to determine the precise surface position of each maplet to a few tenths of a pixel (Fig. 6).

SPC processing (Fig. 7) has been used on small bodies such as asteroids Eros (Thomas et al. 2002) and Itokawa (Gaskell et al. 2006), and large ones such as Mercury (e.g. Tenthoff et al. 2020), Vesta (Gaskell 2012), and Ceres (Park et al. 2019). Psyche is comparable with the Vesta case and as maplets can be located in images at any resolution, illumination and viewing geometry, they provide excellent navigation tie points as well.

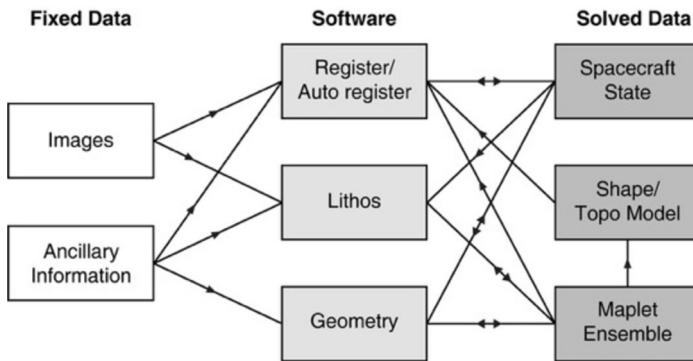


Fig. 7 SPC processing flow from inputs (left) through principal software functions (middle) to products (right). The process is iterative within convergence limits (from Raymond et al. 2011)

An extension of the SPC technique is photoclinometry by deformation (PCD) (i.e. Raymond et al. 2011). This is a technique that allows refinement of shape models or DTMs (“maplets”) derived using other techniques such as stereophotogrammetry and stereophotoclinometry described above. The method is applied to a collection of DTMs, typically the SPC DTMs produced after different orbit altitudes. PCD requires as input the set of DTMs describing the surface of the body, and accurate geometric information derived by the navigation and further refined with the above-mentioned SPC and stereo techniques: the pole orientation, the S/C-object vector in the body-fixed frame and the rotation matrix from the body-fixed frame to the camera frame for each camera image. It also requires input “photometric parameters” allowing calculation of the bi-directional reflectance of the surface; an albedo map can be taken as input. The free parameters of the methods are the heights of the vertices of the DTM above the surface, with the DTM being described as a triangular mesh (“plate model”).

Although it has been successfully applied to the shape model of asteroid Steins (Jorda et al. 2012) and to DTMs of the asteroid Lutetia (Capanna et al. 2012) observed by the OSIRIS cameras aboard ROSETTA, PCD is a newly developed method. It is also a CPU intensive technique. On Dawn, PCD DTMs and derived photometric parameters have been compared to the products of the stereo and SPC processing pipelines successfully (Raymond et al. 2011; Konopliv et al. 2011) and are to be used as inputs to the geodetic DTM. PCD DTMs will also help refine the contributions of brightness variations caused by slope-related surface properties.

4.3 Geodetic-Referenced DTM

The derived models of Psyche’s shape and gravity will be integrated to produce a single combined and internally consistent model of topography and gravity field. The various shape models will be combined using their covariance matrices and statistical estimates of their quality. In addition, radiometric tracking data of the Psyche spacecraft will be re-analyzed using the best gravity model, together with the shape models, for potential improvement of both the shape and gravity. The analysis will be conducted with the GEODYN geophysical estimation program (Rowlands et al. 1993; Pavlis et al. 2001) from imaging data, and Doppler tracking data of various kinds (Zuber et al. 2000, 2022; Neumann et al. 2001). This combination of approaches and solutions will allow parameters to be derived using complementary techniques, thereby offering a potential improvement for the complete geodetic

Table 1 Requirements for optimal and useable observing geometry for SPG and SPC (see also Polansky et al. 2018)

Parameters	Optimal conditions		Useable	
	SPG	SPC	SPG	SPC
Illumination Variation	< 10°	20°–70°	< 15°	10°–85°
Stereo Separation	15°, 15°–65°	0°, 20°–90°	15°, 10°–65°	0°, 15°–90°
Incidence Angle	10°–60°	20°–70°	5°–70°	10°–85°
Emission Angle	< 55°	20°–50°	0°–75°	0°–70°
Phase Angle	5°–90°	0°–90°	5°–90°	0°–90°

and geophysical model of Psyche. The primary objective of this approach is to obtain the best overall topography of Psyche relative to an equipotential surface, with a corresponding gravity field for interpretation of Psyche's interior and dynamics. For more information about gravity see Zuber et al., this issue.

4.4 Observing Requirements for Image-Derived Topography

For stereo imaging the flight system pointing knowledge (i.e., the estimated orientation of the S/C reference frame) should be accurate to 1.5 mrad per axis (3 sigma, zero-to-peak), recorded at least once per second. The Spacecraft System shall provide a resolution of better than 0.005 mrad per axis in its pointing commands and shall be able to point the mounting reference of either imaging camera at a ground-prescribed inertial orientation, with an accuracy of better than 4.65 mrad per axis (3 sigma, zero-to-peak). Note: The accuracy is defined as the total difference between the commanded and actual pointing. Any imaging target should be tracked with an accuracy of better than 5 microrad/sec per axis (3 sigma, zero-to-peak). This includes errors due to tracking rate resolution with a rate resolution of better than 0.25 microrad/sec per axis for tracking rates that it provides to the Flight System. The Spacecraft System shall provide a rate resolution of better than 0.25 microrad/sec per axis in its rate commands.

The stereophotogrammetric method just requires overlapping images from different observation directions. But quality and quantity of the DTM are significantly affected by the imaging and illumination conditions involved. Psyche's stereophotogrammetric observation and illumination requirements are defined based on the experience from stereo processing of other planetary missions, mainly Dawn (Raymond et al. 2011). In a similar manner, conditions that contribute to better accuracy photoclinometrically-derived heights can also be defined (Raymond et al. 2011). Table 1 lists the optimal conditions for each technique, as well as the useable conditions that may not always produce the best height accuracy.

Requirements for SPG, in order of priority:

- the variation of the illumination direction of stereo images should be < 10°, to minimize mis-matching caused by variable illumination. Angles up to 15° are useable.
- the angle between stereo images should be > 15° and < 65°, to provide sufficient vertical and horizontal accuracy. Angles as small as 10° can be used.
- the incidence angle for each image segment should be > 10° and < 60°, to provide sufficient contrast and to minimize the amount of cast shadow areas. Incidence as low as 5° and as high as 70° can be used with care.
- the emission angle for each image segment should be < 55°, to exclude near-limb image segments. Emission as high as 70° can be used, and

- the phase angle for each image segment should be $> 5^\circ$, to avoid influence from opposition effect.

Basic requirements for SPC:

- the variation of the illumination should be $20^\circ\text{--}70^\circ$ ($10^\circ\text{--}85^\circ$ might be useable).
- Nadir image with the emission angle $< 20^\circ$.
- Image in emission angle bins: $20^\circ\text{--}50^\circ$ ($0^\circ\text{--}70^\circ$ might be usable).
- Image in incidence angle bins: $10^\circ\text{--}75^\circ$ (85° might be usable).
- Phase angle $0^\circ\text{--}90^\circ$.
- At least one image with camera azimuth in each of the bins: $0^\circ\text{--}120^\circ$, $120^\circ\text{--}240^\circ$, $240^\circ\text{--}360^\circ$, with a maximum camera azimuth separation between adjacent azimuth bins of no larger than 150° .
- At least two images separated by solar azimuth angle by no less than 150° .

Considering these requirements, it is evident that SPG and SPC techniques are complementary in exploiting different observing conditions, with some overlap. This fits the Psyche mission concept, because the observing geometry is such that both techniques can be used effectively during the mission, as described below

4.5 Imaging Strategy

At Psyche the topographic model will be constructed using data from Orbit B at an altitude of 293 km. Data from other orbits will also be used when appropriate. Psyche's imaging plans include $\sim 19,720$ images in Orbit B (5,916 with the clear filter and a total of 13,804 with the seven color filters), at ~ 15 m pixel scale, each of which covers an area of ~ 600 km². Each image in Orbit B will span a range of phase angles, including angles < 5 degrees. The main phase of multi-angle imaging occurs in the Orbit B phase; multiple complete global mappings with overlapping images are planned. For Orbit B, two nadir and seven off-nadir acquisitions are planned, with a minimum phase angle of 30 degrees.

Psyche will orbit for 20 months. Four coast-only science orbits are foreseen reaching within one body radius in altitude (Fig. 8). Results from each orbit enable final design of, and navigation into, the successive orbits – a method demonstrated by Dawn at both Vesta and Ceres. Each science orbit is designed around a particular driving requirement (for A, gravity for safe navigation to B; for B, topography; for C, gravity science; for D, composition), leaving margins for the other measurements reaching into orders of magnitude (Table 2; Figs. 8 and 9). The downlink budget is sufficient. The science team is organized into both instrument teams and multi-disciplinary working groups supporting requirements definition and data processing.

Psyche is principally a systematic mapping mission to a previously unvisited body. Thus, there are no requirements for targeted observations; nor can the shape and gravity field be characterized sufficiently until arrival. As demonstrated by Dawn (Rayman and Mase 2014; Parcher and Whiffen 2011; Kennedy et al. 2013), close orbiting of a large, unmapped asteroid requires a recursive approach in which science observations in one orbit enable refinement of the gravity field and shape model so as to plan the transfer to the next lower orbit. A key observation strategy for Psyche is the use of multiple-angle images to derive topography for gravity science, and for morphology. This technique perfected by Dawn (Raymond et al. 2011; Polanskey et al. 2012), avoids the need for a laser altimeter on the spacecraft. It does require systematic coverage by overlapping, fixed-off-nadir images, which Psyche's sequence of long-duration orbits provides in abundance. The major imaging requirements are: image pixel scale < 20 m at mean altitude < 400 km; imaging ground track with 20%

Approach: (100 days)

- Optical navigation and instrument calibration
- Hazard assessment (satellite search)
- Psyche spin axis and rotation period measurements

Orbit A: Characterization: 55 days (40 orbits)

- Magnetic field detection
- Nadir mapping for preliminary shape, global color mapping, and gravity field characterization

Orbit B: Topography: 80 days (168 orbits)

- Two Nadir and seven off-nadir imaging cycles for topography (followed by solar conjunction)
- Global color maps, gravity science
- Magnetic field characterization

Orbit C: Gravity Science: 100 days (358 orbits)

- Gravity field mapping
- Continue magnetic field mapping and crater statistics

Orbit D: Elemental Mapping: 100 days (685 orbits)

- Map elemental composition with gamma rays and neutrons
- Continued imaging, gravity, and magnetic field mapping

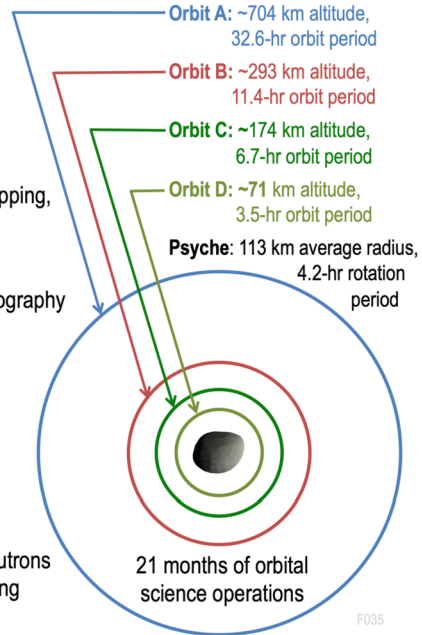


Fig. 8 Psyche science profile uses orbits that progressively improve data quality as knowledge of the gravity field allows lower altitudes (orbit-transfer durations not shown)

Table 2 Relevant orbit parameters yield coverage, resolution & range needed. R/R_p is the ratio of the Psyche spacecraft orbit radius to the Psyche body radius

Science orbit or phase	Ave. altitude (km)	R/R_p	Ave. period (hr)	Inclination	Phase duration (days)	Cycle duration (days)	Repeat cycles/phase	Orbits/repeat cycle	Ave. pixel scale (m)
Approach					100				
Orbit A	704	7.2	32.6	90	55	12.2	4.5	9	35
Transition to Orbit B					18				
Orbit B	293	3.5	11.4	90	80+19	9	9	17	15
Transition to Orbit C					23				
Orbit C	174	2.5	6.7	89	100	14.5	7	49	9
Transition to Orbit D					138				
Orbit D	71	1.7	3.5	160	100	30	3.3	206	4

overlap at equator, for full coverage in one cycle (also achieves gravity coverage requirement); beta angle 30–40°, fixed or slowly varying; Lighting conditions > 80% of the body illuminated or ability to complete coverage later, which will be fulfilled during Orbit B.

Science operations start during the approach phase with an initial assessment of Psyche and its environment using radiometric and optical-image data to estimate spin state, develop a preliminary shape model, calibrate image exposures, and search for orbiting secondaries. At an average altitude of 704 km, Orbit A allows global characterization of the body including first time gravity data; combining these data with the global imaging coverage obtained

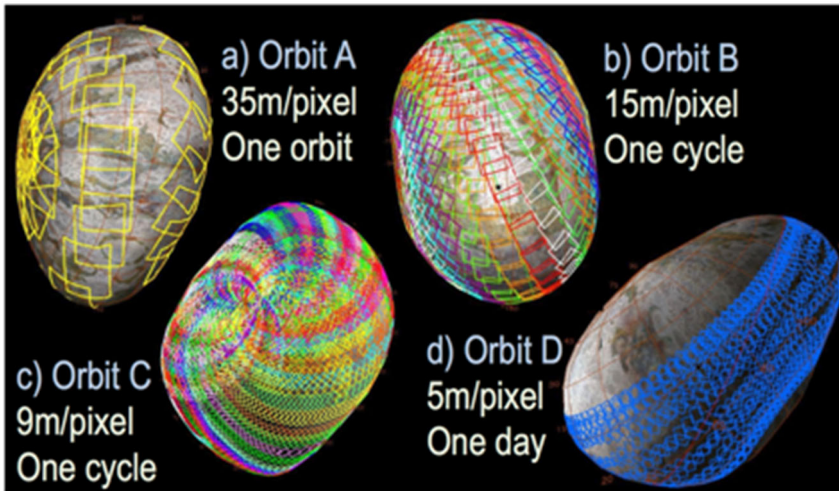


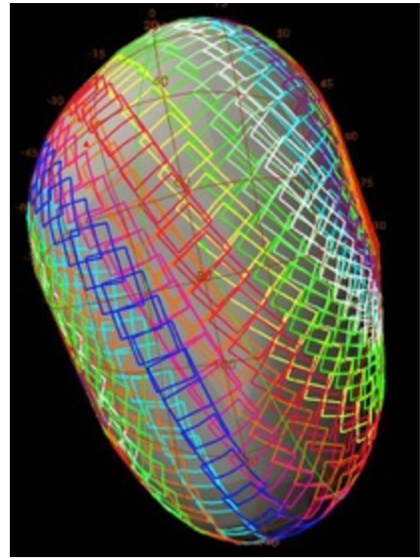
Fig. 9 Resonant Psyche orbits allow superb coverage with routine mapping operations down to Orbit C; stable retrograde Orbit D yields 70% compositional mapping coverage

in this orbit allows to derive the shape-constrained gravity model. A ground-track repeat every 4th cycle would provide complete imaging coverage in a few days. Each cycle generates a complete map of the illuminated hemisphere estimated to exceed 90% of the body based on the currently known pole model, using all eight filters, at 35 m/pixel. The resulting maps and shape model satisfy the geomorphology and color objectives. Figure 9 illustrates the imaging coverage for one mapping orbit. 61 images cover Psyche from terminator to terminator and at least 10% along-track overlap based on Dawn's high-fidelity science planning tools).

Detailed geological mapping using morphological and topographic information enables identification of the geologic context of surface features. Identification of geologic units in terms of morphology, structure, age and compositional heterogeneities is enhanced by information on local relief and the direction of slopes. Relationships of different geologic units define stratigraphic sequences, enabling the identification of relative ages and the modeling of the processes that formed specific surfaces. Topographic measurements are crucial for these investigations and are also used to refine the geodetic control network needed for gravimetric investigations. A comprehensive evaluation of the measurements from the Psyche instruments, based on the image-derived topographic base maps, will enable combined structural/ compositional investigations using the camera and spectrometers.

At Psyche the topographic model will be constructed using data from the Orbit B at a mean planetocentric radius of 399 km. Data from other orbits will also be used when appropriate. Psyche's imaging plans include $\sim 19,720$ images in Orbit B (5,916 with the clear filter and a total of 13,804 with the seven color filters), at ~ 15 m pixel scale, each of which covers an area of ~ 600 km². Each image in Orbit B will span a range of phase angles, including angles < 5 degrees. The main phase of multi-angle imaging occurs in the Orbit B phase; multiple complete global mappings with overlapping images are planned. For Orbit B, two nadir and seven off-nadir acquisitions are planned, with a minimum phase angle of 30 degrees.

Fig. 10 Illustration of the Orbit B ground track for 17 orbits. The imager footprints for each orbit are given a different color and lay down an image swath with overlapping frames that butts against, or overlaps, the neighboring swath



The main topographic mapping data set is obtained in Orbit B. Once the shape models are developed and validated, we will assess them and merge the information with the gravity field to produce the ‘best’ DTM that is referenced to the Psyche center-of-mass.

Global mapping with the imager requires 17 orbits over 8.4 days to complete; the image footprints relative to the ground-track are shown in Fig. 10. The plans for Orbit B include seven off-nadir global mapping cycles and two nadir mappings; each off-nadir global mapping is done at a fixed attitude. The off-nadir angles were chosen such that both techniques will get adequate coverage. The viewing geometry is shown graphically in Fig. 11. Coverage plots for stereo, are shown in Fig. 9, which also illustrates the fact that most data that respect the stereo illumination variation conditions have a very narrow range of illumination, $< 5^\circ$ (bottom panel), which is a natural consequence of the polar sun-synchronous orbit.

In Fig. 12 the stereo coverage plots for SPG and SPC in Orbit B are shown, illustrating the excellent coverage with many useable data. Combining both data set will result in the required stereo coverage of 80% which meet the mission requirements.

In addition, the combination of SPG and SPC improves the topographic resolution significantly (Fig. 13) as demonstrated by Dawn results of Ceres (Neesemann et al. 2022).

Topographic maps are produced using the stereo photogrammetry (SPG) and stereo photoclinometry (SPC) techniques developed by Dawn [Raymond et al. 2011; Polanskey et al. 2012]; The topography model from clear-filter images taken from multiple view angles using one imager at a time. The spacecraft is nadir-pointed for the first and fifth mapping cycles; and at a fixed off-nadir attitude for the rest. Each mapping cycle uses one fixed off-nadir angle. The set of angles for the series optimizes among multiple factors: stereo separation between image pairs ($\geq 15^\circ$); and incidence, emission, and phase angles. Four ground-track repeat cycles, taking 33.6 d total in Orbit B, are required to meet the topography objective; five additional cycles are added for margin, driving the science portion of Orbit B to 80 d total. The spacecraft ground track provides uniform coverage with 20% overlaps between imaging swaths. The lighting conditions and data budget allow 99% of the surface to be mapped in Orbit B. In order to verify the coverage, the received images will be georectified based on the preliminary shape model and mosaicked immediately after each download to support operations planning (Fig. 14).

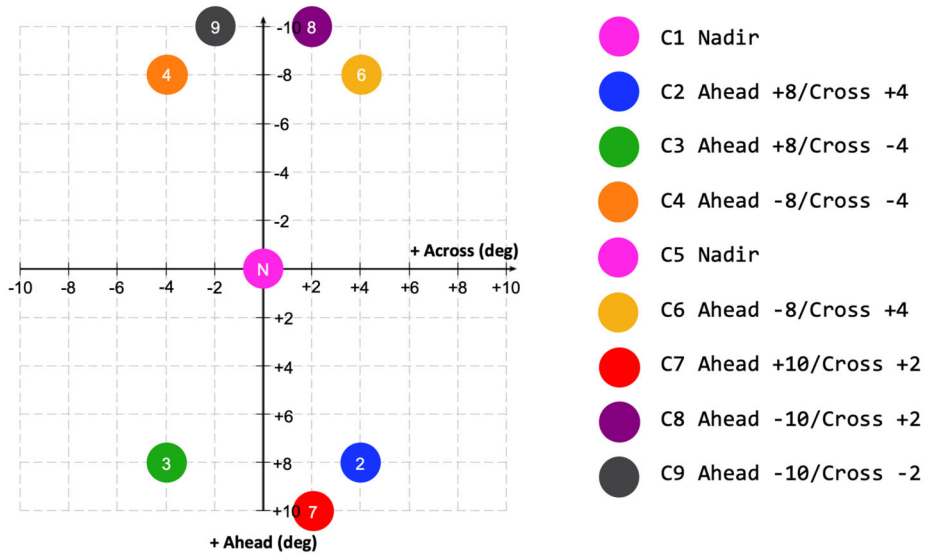


Fig. 11 Illustration of the off nadir viewing geometry as referenced to spacecraft coordinates for the nine global mapping cycles (Polanskey et al. 2022). For a polar orbit, constant illumination is in the “Ahead” direction, while maximum illumination variation is achieved in the “Cross” direction. The angles in the Cross direction are maximized within the constraints of keeping on the body and achieving proper incidence and emission angles

5 Data Products

The following high-level products will be produced:

1. local, regional, and global Digital Terrain Models (DTMs)
2. local, regional, and global clear filter mosaics
3. local, regional, and global color mosaics

Figure 15 shows the tiling scheme for quadrangle mapping used for the Dawn mission.

The Psyche coordinate system will be defined in two steps. In close cooperation with the IAU, a tiny crater near the equator will be selected to define the longitude system. Next, the rotation axis and period are determined during the photogrammetric processing of the stereo images. Together these will define the coordinate system. The east longitude system will be used and the thematic convention for naming craters and other features will be defined in close cooperation with the IAU. The Psyche topographic atlas will be produced in a scale of 1:250,000 or 1:500,000 and will consist of 15 tiles that conform to the quadrangle scheme. This tiling schema was recently used for the Saturnian satellites like Enceladus and Vesta and Ceres (Roatsch et al. 2012, 2013, 2016).

Detailed geological mapping using morphological and topographic information enables identification of the geologic context of surface features. Identification of geologic units in terms of morphology, structure, age and compositional heterogeneities is enhanced by information on local relief and the direction of slopes. Relationships of different geologic units define stratigraphic sequences, enabling the identification of relative ages and the modeling of the processes that formed specific surfaces. Topographic measurements are crucial for these investigations and are also used to refine the geodetic control network needed for

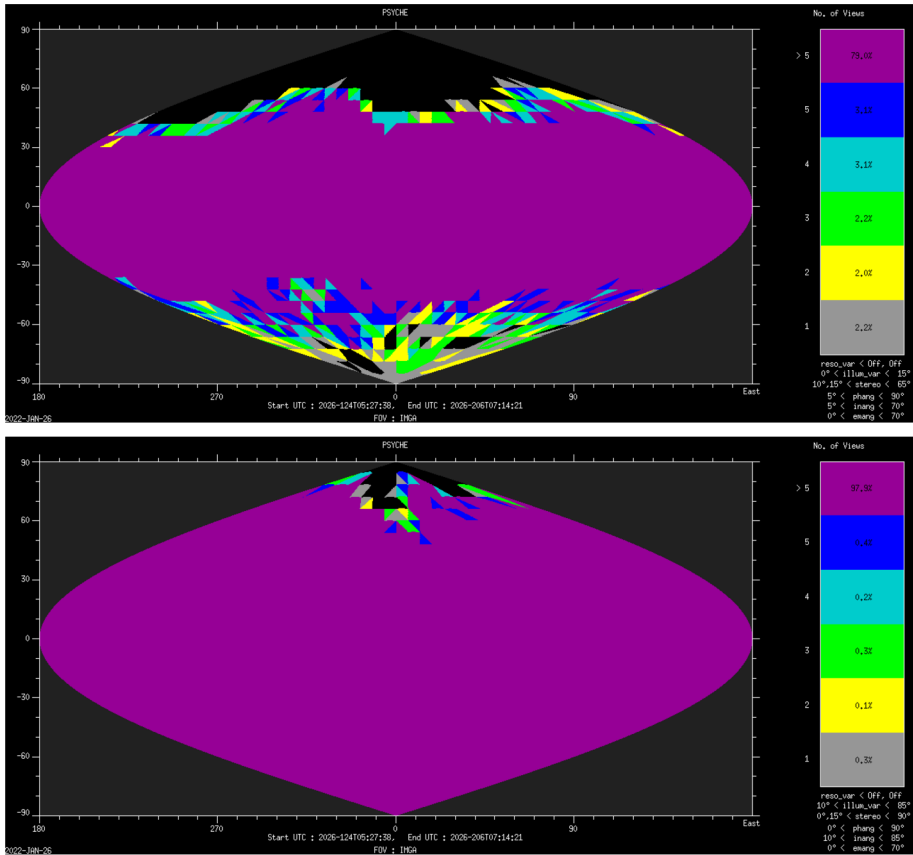


Fig. 12 In Orbit B, SPG coverage meets the useable stereo conditions for incidence angle up to 70° (top) and resolutions of 10 m/pixel – 20 m/pixel. The bottom plot shows the coverage for SPC in Orbit B with the same resolution. The colors indicate the number of independent datums in each $.25^\circ$ bin that collectively meet the criteria outlined in Table 1. The area covered at a given number of views is indicated by the percentage number in the legend

gravimetric investigations. A comprehensive evaluation of the measurements from the Psyche instruments, based on the image-derived topographic base maps, will enable combined structural/compositional investigations using the camera and spectrometers

A geologic mapping campaign for asteroid Psyche will be performed during the approximately two-year (21 month) nominal mission which will result in a global geologic map of Psyche at a map scale of 1:500,000. This map scale is based on the size of Psyche (geometric mean diameter of 186 km). However, given the Orbit B image spatial resolution of ~ 15 m/pixel, the digital geologic mapping of Psyche can be done at a map scale as high as 1:60,000. Depending upon the variety and types of surface features discovered on Psyche, additional regional/local geologic maps as needed/justified by the geology of Psyche will be produced, in which cartographic image maps and DTMs are used as our mapping bases. As was done with Vesta and Ceres, geologic mapping will be done digitally using ArcGISTM software and in consultation with mapping specialists from the U.S. Geological Survey, using community standards (i.e., Skinner et al. 2018).

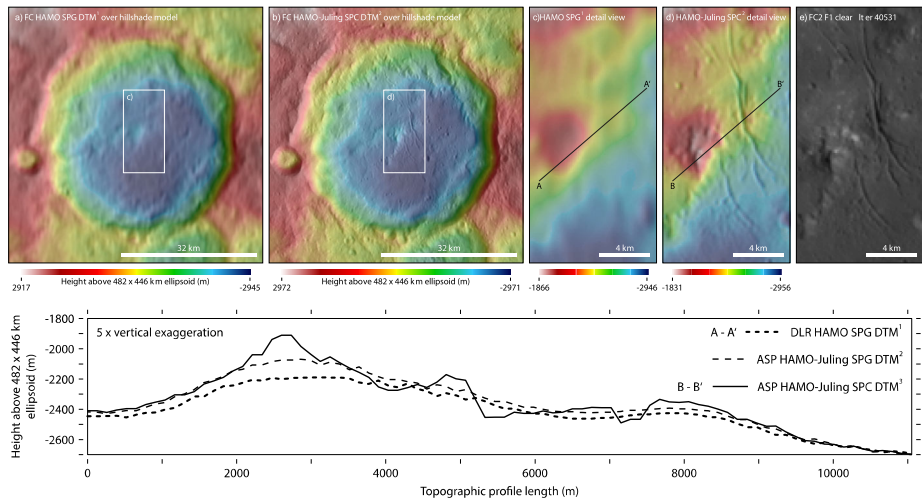


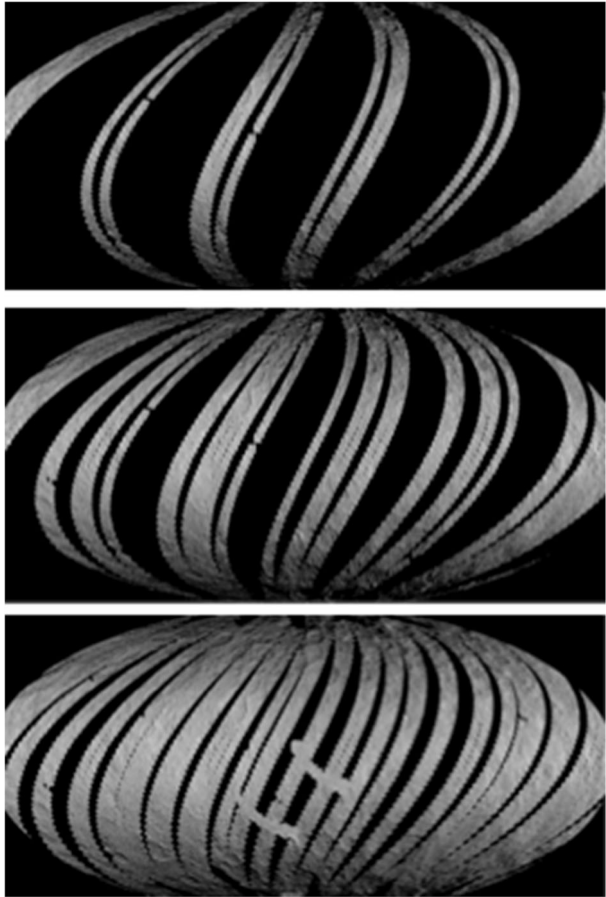
Fig. 13 Topography of Azacca impact crater on Ceres based on Dawn Framing Camera (FC) observations. (a) The SPG DTM as derived from HAMO data. (b) FC HAMO and Juling 1 orbit frames bundle adjusted and photometric corrected frames SPG processed, followed by SPC processing. This combination allows topographic resolutions as of the HAMO input frames ($\sim 136\text{--}140$ m/pixel). (c, d, e) Show subsets of the central peak and the topographic cross section illustrate the improvement of the SPG and SPC combination

Geological mapping of a new planetary object with a totally different surface will arise new issues. Like that used for asteroid (4) Vesta on the Dawn mission surface features will be identified during approach and refined during the first orbital phase (Russell et al. 2015). Based on modeled processes of solidification possible for a stripped, molten metal core the following developed hypotheses for features are expected on Psyche's surface (see also Elkins-Tanton et al. 2020):

- Scarps, perhaps on the order of 10 km tall, from contraction of the body.
- Sulfur-rich lava flows from the original solidification and liquid expulsion.
- Craters of all sizes and perhaps with different morphologies depending on whether they occurred on the warm or cold side of Psyche.
- Slabs, probably on the order of 100 km scale, of achondritic original mantle material from the Psyche parent body that fell back onto the surface during stripping.
- Exogenic chondritic silicate deposits delivered by impactors.

At present it is unclear how these and other features will look on a metallic object. For example, one might expect a harder metallic surface to be more resistant to the effects of space weathering, such that the surface could have less regolith than silicate objects have. We will follow standard best geological mapping practices to define and characterize the surface into geologic units based on physical attributes (morphology, albedo, color, texture, contact relations with neighboring units and mainly topography), and then work to interpret these features in terms of all the possible geologic processes that might produce them (e.g. Jaumann et al. 2012; Buczowski et al. 2016). As the spacecraft enters lower orbits and spatial resolution of images improve, it is likely (as we found at Vesta) that one or more hypotheses regarding formation processes for some geologic units can be eliminated (e.g. Jaumann et al. 2012; Buczowski et al. 2016). This would improve our understanding of the geology of Psyche and enable us to derive its geologic history. Hypothetical surface

Fig. 14 Example of Dawn Ceres coverage verification



features expected on Psyche are also known on Earth and other previously mapped solar system bodies. Contraction scarps, surface expression of thrust faults, where the crust is broken along an inclined plane and pushed upward are observed on Mercury (e.g. Watters 2021) and the Moon (e.g. Banks et al. 2012) and Earth (e.g. Plescia and Golombek 1986). Sulfur-rich lava flows exist on Io (e.g. Lopes 2007), and lava flows consisting primarily of calcium occur on Earth in Africa (Bondre 2008). However, despite of the abundance of basalt on Vesta lava flows were not identified due to regolith and ejecta burial (e.g. Russell et al. 2015). The same effect might obscure possible lava flows on Psyche while spectroscopic observation might detect basaltic compositions. As exogenic silicates (e.g. Le Corre et al. 2015) delivered by impactors have also already been mapped on Vesta and the Moon, this should also be expected on Psyche (Elkins-Tanton et al. 2020).

6 Expected Results

Imagery contributes to many of Psyche's scientific objectives, often in combination with other complementary data sets. For example, the average density is calculated from the volume as measured by the camera and the mass is derived from radio science. The prime task

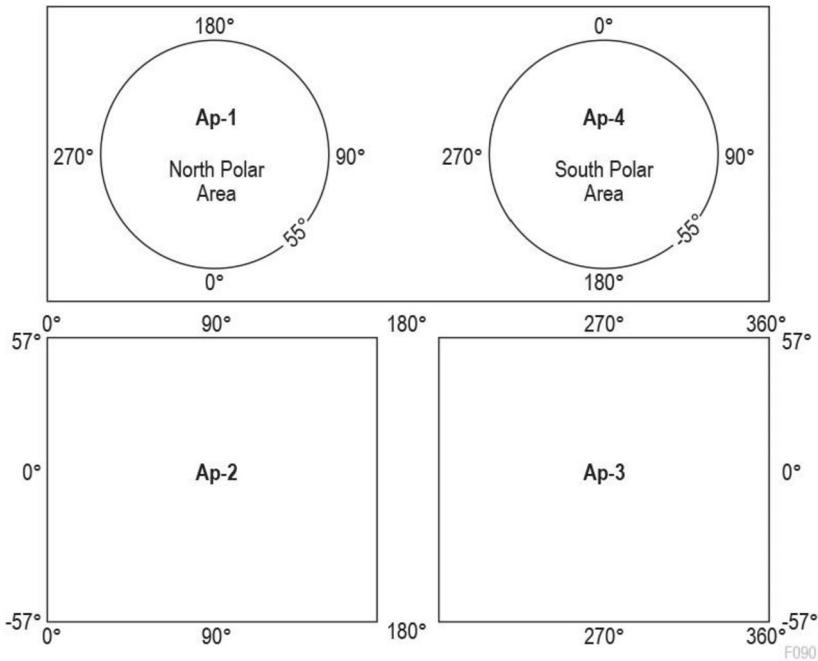


Fig. 15 4-quadrangle tiling scheme of the Psyche topographic atlas

of the camera is to image (map) the surface of Psyche in high spatial resolution, under various illumination conditions and from multiple directions, and in different spectral bands. The images are then combined into mosaics for each spectral band, thus presenting an important tool for the study and analysis of the geomorphology and decipher the geological history and the evolution of the surface. Imaging will be performed from far-field global maps to local-site characterization under various observing geometries and lighting conditions yielding surface resolution of about 15 m/pixel globally and a few m/pixel locally comparable what was achieved by the Dawn mission (e.g. Raymond et al. 2011; Russell et al. 2015). The analysis of geomorphologic features (down to the scale of a few 10's of meters in the high-resolution phase yields exclusive evidence on the different geologic processes responsible for the state of the surfaces, including impact cratering, tectonism, gradation (weathering, erosional, and depositional features like mass movements) and possible volcanism (e.g. Jaumann et al. 2012; Russell et al. 2015; Schmedemann et al. 2014; Williams et al. 2014; Buczkowski et al. 2016; Hiesinger et al. 2016). Clues to the formation age of surface units and its stratigraphy can be derived from the frequency-size distribution of craters, their morphology and interior structure, all of which requires topographic information (e.g. Schmedemann et al. 2014; Williams et al. 2014; Hiesinger et al. 2016). The vertical accuracy of the stereo data is like the spatial pixel resolution that allows a detailed 3-dimensional analysis of surface features (e.g. Raymond et al. 2011; Jaumann et al. 2012; Preusker et al. 2016). Multispectral images allow mapping compositional surface variations (e.g. De Sanctis et al. 2013, 2016; Ammannito et al. 2016), whereas multi-angle images provide hints to the textural properties of the regolith and the surface roughness (e.g. Schroeder et al. 2013).

Slopes of movable surface material are determined not just by the geologic processes that create topography, but by the nature of the material (regolith) (e.g. Pieters et al. 2012) and the gravity (e.g. Konopliv et al. 2011) of the body. Knowledge of the magnitudes as well as directions of slopes is needed to answer questions about the viscosities and strengths, and hence the possible composition of materials (e.g. Duarte et al. 2019). Information of the physical surface properties by the means of multi-phase angle observations also supports the geologic context characterization (e.g. Schroeder et al. 2013). The major result of these studies is the identification of geologic units in terms of morphology, structure, age, and compositional heterogeneities with evidence of the presence of local relief. The relationship of different geologic units will build up stratigraphic sequences, which are used to model the processes that formed the specific surface (e.g. Williams et al. 2014). Stereoscopic measurements are crucial for these investigations and are also used to refine the geodetic control network and thus support gravimetric investigations (e.g. Konopliv et al. 2011).

The shapes of craters on Psyche will be of great interest, especially if there are large areas of metal (see also Marchi et al., this issue). Each body in the solar system has yielded new examples and types of shapes of impact craters, and craters on asteroids have been particularly interesting. For example, Vesta has many ‘asymmetric craters’, formed by impacts on steep slopes, which results in sharp upslope crater rim, and a muted downslope crater rim (because of preferential accumulation of ejecta downslope) (Jaumann et al. 2012; Krohn et al. 2014). The angle of repose of freely moving grains is higher on smaller bodies: lesser gravity allows grains to pile at higher angles before slipping down. This means that where regolith is formed on asteroids, we can expect it to pile into steeper slopes than we are used to seeing on Earth. If a metal substrate can form a regolith is unknown and on Psyche regolith may be mainly rocky material, either native or delivered by later impacts. Slopes as estimated by topographic analysis will therefore constrain the nature of surface material. Shaking from impacts and sliding on hillslopes may sort the material.

Impact crater on asteroids like Vesta and Ceres show related fracturing of different occurrence. Global fracture systems induced by large impacts dominate Vesta (Jaumann et al. 2012; Buczkowski et al. 2012), impact related fracture systems on Ceres show concentric and radial fractures which are interpreted due to creep of low viscosity subsurface layers or upwelling processes (Otto et al. 2019). Another impact related fracture system are concentric or radial floor-fracture craters on Ceres due to mechanisms include cooling/melting processes, degassing, and subsidence of the crater floor by up-doming of subsurface material because of absolute tensile stresses (Krohn et al. 2020). The spin of asteroids evolves due to collisions (e.g. Mao and McKinnon 2020) and thus may imply fracturing (e.g. Fu et al. 2014, 2017; Otto et al. 2016). Impact induced fracturing as observed on Vesta might also occur on Psyche while the volatile related fracturing as observed on Ceres is rather unlikely (see also Marchi et al. 2022 this issue; Zuber et al. 2022 this issue).

A comprehensive evaluation of the measurements from instruments based on the stereo derived topographic image base maps will improve the overall mission output by combined structural/compositional investigations using the camera and spectrometer. The high-resolution digital shape models are derived using various techniques and merged into a geodetically controlled topographic model will enable investigation of the geology expected on Psyche. Slumps and landslides can be identified and tied to source regions. Craters will be well resolved topographically, and their degradation states revealed. The high-resolution slope data will enable brightness variations to be confidently identified and related to spectral variations in terms of composition, grain sizes, or other factors. Psyche’s high-resolution topographic models, together with the gravity data will enable co-registration of data sets to determine the geologic history.

Acknowledgements The authors are grateful for the experience gained with the Dawn project. A portion of this work was performed at the Jet Propulsion Laboratory, California Institute of Technology, the Freie Universitaet Berlin and the Arizona State University in Tempe.

Funding Note Open Access funding enabled and organized by Projekt DEAL.

Open Access This article is licensed under a Creative Commons Attribution 4.0 International License, which permits use, sharing, adaptation, distribution and reproduction in any medium or format, as long as you give appropriate credit to the original author(s) and the source, provide a link to the Creative Commons licence, and indicate if changes were made. The images or other third party material in this article are included in the article's Creative Commons licence, unless indicated otherwise in a credit line to the material. If material is not included in the article's Creative Commons licence and your intended use is not permitted by statutory regulation or exceeds the permitted use, you will need to obtain permission directly from the copyright holder. To view a copy of this licence, visit <http://creativecommons.org/licenses/by/4.0/>.

References

- E. Ammannito, M.C. DeSanctis, M. Ciarniello, A. Frigeri, F.G. Carrozzo, J.-Ph. Combe, B.L. Ehlmann, S. Marchi, H.Y. McSween, A. Raponi, M.J. Toplis, F. Tosi, J.C. Castillo-Rogez, F. Capaccioni, M.T. Capria, S. Fonte, M. Giardino, R. Jaumann, A. Longobardo, S.P. Joy, G. Magni, T.B. McCord, L.A. McFadden, E. Palomba, C.M. Pieters, C.A. Polansky, M.D. Rayman, C.A. Raymond, P.M. Schenk, F. Zambon, C.T. Russell, Distribution of phyllosilicates on the surface of Ceres. *Science* **353**, 1006 (2016). <https://doi.org/10.1126/science.aaf4279>
- M.E. Banks, T.R. Watters, M.S. Robinson, L.L. Tornabene, T. Tran, L. Ojha, N.R. Williams, Morphometric analysis of small-scale lobate scarps on the Moon using data from the Lunar Reconnaissance Orbiter. *J. Geophys. Res.* **117**, E00H11 (2012). <https://doi.org/10.1029/2011JE003907>
- N. Bondre, Molten carbonate eruptions. *Nat. Geosci.* **1**, 498 (2008). <https://doi.org/10.1038/ngeo274>
- D.T. Britt, C.M. Pieters, Bidirectional reflectance properties of iron-nickel meteorites, in *Lunar and Planetary Science Conference 18* (1988)
- D.L. Buczkowski, D.Y. Wyrick, K.A. Iyer, E.G. Kahn, J.E.C. Scully, A. Nathues, R.W. Gaskell, T. Roatsch, F. Preusker, P.M. Schenk, L. Le Corre, V. Reddy, R.A. Yingst, S. Mest, D. Williams, W.B. Garry, O.S. Barnouin, R. Jaumann, C.A. Raymond, C.T. Russell, Large-scale troughs on Vesta: a signature of planetary tectonics. *Geophys. Res. Lett.* **39**(17), L18205 (2012). <https://doi.org/10.1029/2012GL052959>
- D.L. Buczkowski, D.Y. Wyrick, M. Toplis, R.A. Yingst, D.A. Williams, W.B. Garry, S. Mest, T. Kneissl, S.E.C. Scully, A. Nathues, M.C. De Sanctis, L. LeCorre, V. Reddy, M. Hoffmann, E. Ammannito, A. Frigeri, F. Tosi, F. Preusker, T. Roatsch, C.A. Raymond, R. Jaumann, C.M. Pieters, C.T. Russell, The unique geomorphology and physical properties of the Vestalia Terra plateau. *Icarus* **244**, 89–103 (2014). <https://doi.org/10.1016/j.icarus.2014.03.035>
- D.L. Buczkowski, B.E. Schmidt, D.A. Williams, S.C. Mest, J.E.C. Scully, A.I. Ermakov, F. Preusker, P. Schenk, K.A. Otto, H. Hiesinger, D. O'Brien, S. Marchi, H. Sizemore, K. Hughson, H. Chilton, M. Bland, S. Byrne, N. Schorghofer, T. Platz, R. Jaumann, T. Roatsch, M.V. Sykes, A. Nathues, M.C. De Sanctis, C.A. Raymond, C.T. Russell, The geomorphology of Ceres. *Science* **353**, 1004 (2016). <https://doi.org/10.1126/science.aaf4332>
- C. Capanna, L. Jorda, G. Gesquière, P. Lamy, M. Kaasalainen, Lutetia global shape and topography reconstructed with photogrammetry by deformation. Vol. 7, EPSC2012-616 (2012)
- M.T. Capria, F. Tosi, M.C. De Sanctis, F. Capaccioni, E. Ammannito, A. Frigeri, F. Zambon, S. Fonte, E. Palomba, D. Turrini, T.N. Titus, S.E. Schröder, M. Toplis, J.-Y. Li, J.-P. Combe, C.A. Raymond, C.T. Russell, Vesta surface thermal properties map. *Geophys. Res. Lett.* **41**, 1438–1443 (2014). <https://doi.org/10.1002/2013GL059026>
- J.M. Christoph, T. Sharp, S. Marchi, L.T. Elkins-Tanton, Characterizing ejecta fragments from impact experiments into meteoric iron using scanning electron microscopy (SEM), in *LPSC 52 Abstract #2730* (2021)
- E.A. Cloutis, M.J. Gaffey, D.G. Smith, R.S.J. Lambert, Metal silicate mixtures: spectral properties and applications to asteroid taxonomy. *J. Geophys. Res.* **95**, 8323–8338 (1990a)
- E.A. Cloutis, M.J. Gaffey, D.G. Smith, R.S.J. Lambert, Reflectance spectra of “featureless” materials and the surface mineralogies of M- and E-class asteroids. *J. Geophys. Res.* **95**(B1), 281–293 (1990b)

- M.C. De Sanctis, E. Ammannito, M.T. Capria, F. Tosi, F. Capaccioni, F. Zambon, F. Carraro, S. Fonte, A. Frigeri, R. Jaumann, G. Magni, S. Marchi, T.B. McCord, L.A. McFadden, H.Y. McSween, D.W. Mittlefehldt, A. Nathues, E. Palomba, C.M. Pieters, C.A. Raymond, C.T. Russell, M.J. Toplis, D. Tur-rini, Spectroscopic characterization of mineralogy and its diversity across Vesta. *Science* **336**, 697–700 (2012). <https://doi.org/10.1126/science.1219270>
- M.C. De Sanctis, E. Ammannito, T.M. Capria, F. Capaccioni, J.-P. Combe, A. Frigeri, A. Longobardo, G. Magni, S. Marchi, T.B. McCord, E. Palomba, F. Tosi, F. Zambon, F. Carraro, S. Fonte, J.-Y. Li, L.A. McFadden, D.W. Mittlefehldt, C.M. Pieters, R. Jaumann, K. Stephan, C.A. Raymond, C.T. Russell, Vesta's mineralogical composition as revealed by the visible and infrared spectrometer on Dawn. *Meteorit. Planet. Sci.* **48**(11), 2166–2184 (2013). <https://doi.org/10.1111/maps.12138>
- M.C. De Sanctis, A. Raponi, E. Ammannito, M. Ciarniello, M.J. Toplis, H.Y. McSween, J.C. Castillo-Rogez, B.L. Ehlmann, F.G. Carrozzo, S. Marchi, F. Tosi, F. Zambon, F. Capaccioni, M.T. Capria, S. Fonte, M. Formisano, A. Frigeri, M. Giardino, A. Longobardo, G. Magni, E. Palomba, L. McFadden, C.M. Pieters, R. Jaumann, P. Schenk, R. Mugnuolo, C.A. Raymond, C.T. Russell, Bright carbonate deposits as evidence of aqueous alteration on (1) Ceres. *Nature* **536**, 54–57 (2016). <https://doi.org/10.1038/nature18290>
- M. Delbo, G. Libourel, J. Wilkerson et al., Thermal fatigue as the origin of regolith on small asteroids. *Nature* **508**, 233–236 (2014). <https://doi.org/10.1038/nature13153>
- B.W. Denevi, A.W. Beck, E.I. Coman, B.J. Thomson, E. Ammannito, D.T. Blewett, J.M. Sunshine, M.C. De Sanctis, J.-Y. Li, S. Marchi, D.W. Mittlefehldt, N.E. Petro, C.A. Raymond, C.T. Russell, Global variations in regolith properties on asteroid Vesta from Dawn's low-altitude mapping orbit. *Meteorit. Planet. Sci.* **51**, 2366–2386 (2016). <https://doi.org/10.1111/maps.12729>
- K.D. Duarte, B. Schmidt, H. Chilton, K. Hughson, H. Sizemore, K.L. Ferrier, J. Buffo, J. Scully, A. Nathues, T. Platz, M. Landis, S. Byrne, M. Bland, C.T. Russell, C.A. Raymond, Landslides on Ceres: diversity and geologic context. *J. Geophys. Res., Planets* **124**, 3329–3343 (2019). <https://doi.org/10.1029/2018JE005673>
- L.T. Elkins-Tanton, E. Asphaug, J.F. Bell III, H. Bercovici, B. Bills, R. Binzel et al., Observations, meteorites, and models: a preflight assessment of the composition and formation of (16) Psyche. *J. Geophys. Res., Planets* **125**, e2019JE006296 (2020). <https://doi.org/10.1029/2019JE006296>
- A.I. Ermakov, M. Kreslavsky, J.E.C. Scully, K.H.G. Hughson, R.S. Park, Surface roughness and gravitational slope distributions of Vesta and Ceres. *J. Geophys. Res., Planets* **124**, 14–30 (2019). <https://doi.org/10.1029/2018JE005813>
- M. Ferrais, P. Vernazza, L. Jorda, N. Rambaux, J. Hanuš, B. Carry, F. Marchis, M. Marsset, M. Viikinkoski, M. Brož, R. Fetick, A. Drouard, T. Fusco, M. Birlan, E. Podlowska-Gaca, E. Jehin, P. Bartczak, J. Berthier, J. Castillo-Rogez, F. Cipriani, F. Colas, G. Dudziński, C. Dumas, J. Durech, M. Kaasalainen, A. Kryszczyńska, P. Lamy, H. Le Coroller, A. Marciniak, T. Michalowski, P. Michel, T. Santana-Ros, P. Tanga, F. Vachier, A. Vigan, O. Witasse, B. Yang, Asteroid (16) Psyche's primordial shape: a possible Jacobi ellipsoid. *Astron. Astrophys.* **638**, L15 (2020). <https://doi.org/10.1051/0004-6361/202038100>
- A. Figeri, M.C. De Sanctis, E. Ammannito, F. Tosi, A. Longobardo, F. Zambon, T. McCord, J.P. Combe, R. Jaumann, C.A. Raymond, C.T. Russell, The spectral parameter maps of Vesta from VIR data. *Icarus* **259**, 10–20 (2015). <https://doi.org/10.1016/j.icarus.2015.06.027>
- H. Fossen, G. Carolina, G. Cavalcante, R. Vizeu, L. Pinheiro, C.J. Archanjo, Deformation – progressive or multiphase? *J. Struct. Geol.* **125**, 82–99 (2019). <https://doi.org/10.1016/j.jsg.2018.05.006>
- R.R. Fu, B.H. Hager, A.I. Ermakov, M.T. Zuber, Efficient early global relaxation of asteroid Vesta. *Icarus* **240**, 133–145 (2014)
- R.R. Fu, A.I. Ermakov, S. Marchi, J.C. Castillo-Rogez, C.A. Raymond, B.H. Hager, M.T. Zuber, S.D. King, M.T. Bland, M.C. De Sanctis, F. Preusker, R.S. Park, C.T. Russell, The interior structure of Ceres as revealed by surface topography. *Earth Planet. Sci. Lett.* **476**, 153–164 (2017)
- R. Gaskell, SPC shape and topography of Vesta from DAWN imaging data, in *AAS, DPS XLIV, 209.03* (2012)
- R. Gaskell, J. Saito, M. Ishiguro, T. Kubota, T. Hashimoto, N. Hirata, S. Abe, O.S. Barnouin-Jha, D. Scheeres, Global topography of asteroid 25143 Itokawa, in *LPSC 37 Abstract #1826* (2006)
- R.W. Gaskell, O.S. Barnouin-Jha, D.J. Scheeres, A.S. Konopliv, T. Mukai, S. Abe, J. Saito, M. Ishiguro, T. Kubota, T. Hashimoto, J. Kawaguchi, M. Yoshikawa, K. Shirakawa, T. Kominato, N. Hirata, H. Demura, Characterizing and navigating small bodies with imaging data. *Meteorit. Planet. Sci.* **43**, 1049–1062 (2008)
- K. Gwinner, F. Scholten, M. Spiegel, R. Schmidt, B. Giese, J. Oberst, C. Heipke, R. Jaumann, G. Neukum, Derivation and validation of high-resolution digital terrain models from Mars Express HRSC data. *Photogramm. Eng. Remote Sens.* **75**(9), 1127–1142 (2009)
- K. Gwinner, R. Jaumann, H.H. Hauber, C. Heipke, J. Oberst, G. Neukum, V. Ansan, J. Bostelmann, A. Dumke, S. Elgner, G. Erkeling, F. Fueten, N.M. Hoekzema, E. Kersten, D. Loizeau, D.-D. Matz, V. Mertens, G. Michael, A. Pasewaldt, P. Pinet, F. Preusker, D. Reiss, T. Roatsch, R. Schmidt, F. Scholten,

- M. Spiegel, R. Stesky, D. Tirsch, S. van Gasselt, M. Wählisch, K. Willner, The high resolution stereo camera (HRSC) of Mars Express and its approach to science analysis and mapping for Mars and its satellites. *Planet. Space Sci.* **196**, 93–138 (2016). <https://doi.org/10.1016/j.pss.2016.02.014>
- D. Haack, K. Otto, B. Gundlach, C. Kreuzig, D. Bischoff, E. Kührt, J. Blum, Tensile strength of dust-ice mixtures and their relevance as cometary analog material. *Astron. Astrophys.* **642**, A218 (2020). <https://doi.org/10.1051/0004-6361/202037763>
- M.D. Hicks, B.J. Buratti, K.J. Lawrence, J. Hillier, J.-Y. Li, V. Reddy, S. Schröder, A. Nathues, M. Hoffmann, L. Le Corre, R. Duffard, H.-B. Zhao, C. Raymond, C. Russell, T. Roatsch, R. Jaumann, H. Rhoades, D. Mayes, T. Barajas, T.-T. Truong, J. Foster, A. McAuley, Spectral diversity and photometric behavior of main-belt and near-Earth vasteroids and (4) Vesta: a study in preparation for the Dawn encounter. *Icarus* **235**, 60–74 (2014). <https://doi.org/10.1016/j.icarus.2013.11.011>
- H. Hiesinger, S. Marchi, N. Schmedemann, P. Schenk, J.H. Pasckert, A. Neesemann, D.P.O. Brien, T. Kneissl, A.I. Ermakov, R.R. Fu, M.T. Bland, A. Nathues, T. Platz, D.A. Williams, R. Jaumann, J.C. Castillo-Rogez, O. Ruesch, B. Schmidt, R.S. Park, F. Preusker, D.L. Buczkowski, C.T. Russell, C.A. Raymond, Cratering on Ceres: implications for its crust and evolution. *Science* **353**, 1003 (2016). <https://doi.org/10.1126/science.aaf4759>
- T. Hiroi, C.M. Pieters, H. Takeda, Grain size of the surface regolith of asteroid 4 Vesta estimated from its reflectance spectrum in comparison with HED meteorites. *Meteoritics* **29**, 394–396 (1994). <https://doi.org/10.1111/j.1945-5100.1994.tb00603.x>
- R. Jaumann, G. Neukum, T. Behnke, T.C. Duxbury, K. Eichertopf, J. Flohrer, S.v. Gasselt, B. Giese, K. Gwinner, E. Hauber, H. Hoffmann, A. Hoffmeister, U. Köhler, K.-D. Matz, T.B. McCord, V. Mertens, J. Oberst, R. Pischel, D. Reiss, E. Ress, T. Roatsch, P. Saiger, F. Scholten, G. Schwarz, K. Stephan, M. Wählisch (the HRSC Co-Investigator Team), The high-resolution stereo camera (HRSC) experiment on Mars Express: instrument aspects and experiment conduct from interplanetary cruise through the nominal mission. *Planet. Space Sci.* **55**, 928–952 (2007)
- R. Jaumann, D.A. Williams, D.L. Buczkowski, R.A. Yingst, F. Preusker, H. Hiesinger, N. Schmedemann, T. Kneisl, J.B. Vincent, D.T. Blewett, B.J. Buratti, U. Carsenty, B.W. Denevi, M.C. De Sanctis, W.B. Garry, H.U. Keller, E. Kersten, K. Krohn, J. Li, S. Marchi, K.D. Matz, T.B. McCord, H.Y. McSween, S.C. Mest, D.W. Mittlefehldt, S. Mottola, A. Nathues, G. Neukum, D.P. O'Brien, C.M. Pieters, T.H. Prettyman, C.A. Raymond, T. Roatsch, C.T. Russell, P. Schenk, B.E. Schmidt, F. Scholten, K. Stephan, M.V. Sykes, P. Tricarico, R. Wagner, M.T. Zuber, H. Sierks, Vesta's shape and morphology. *Science* **336**, 687–690 (2012). <https://doi.org/10.1126/science.1219122>
- B.C. Johnson, M.M. Sori, A.J. Evans, Ferrovulcanism on metal worlds and the origin of pallasites. *Nat. Astron.* **4**, 41–44 (2020). <https://doi.org/10.1038/s41550-019-0885-x>
- L. Jorda, P.L. Lamy, R.W. Gaskell, M. Kaasalainen, O. Groussin, S. Besse, G. Faury, Asteroid (2867) Steins: shape, topography and global physical properties from OSIRIS observations. *Icarus* **221**, 1089–1100 (2012). <https://doi.org/10.1016/j.icarus.2012.07.035>
- M. Jutzi, E. Asphaug, Mega-ejecta on asteroid Vesta. *Geophys. Res. Lett.* **38**, L01102 (2011). <https://doi.org/10.1029/2010GL045517>
- M. Jutzi, E. Asphaug, P. Gillet, J.A. Brarrat, W. Benz, The structure of the asteroid 4 Vesta as revealed by models of planet-scale collisions. *Nature* **494**, 207–210 (2013). <https://doi.org/10.1038/nature11892>
- B. Kennedy, M. Abrahamson, A. Ardito, D. Han, R. Haw, N. Mastrodemos, S. Nandi, R. Park, B. Rush, A. Vaughan, Dawn orbit determination team: trajectory and gravity prediction performance during Vesta science phases, in *Paper AAS 2013-345, 23rd AAS/AIAA Spaceflight Mechanics Meeting*, Kauai, Hawaii, Feb. 10–14, 2013 (2013)
- M.G. Kleinhans, H. Markies, S.J. de Vet, A.C. In 't Veld, F.N. Postema, Static and dynamic angles of repose in loose granular materials under reduced gravity. *J. Geophys. Res.* **116**, E11004 (2011). <https://doi.org/10.1029/2011JE003865>
- A.S. Konopliv, S.W. Asmar, F.G. Bills, N. Mastrodemos, R.S. Park, C.A. Raymond, D.E. Smith, M.T. Zuber, The dawn gravity investigation at Vesta and Ceres. *Space Sci. Rev.* **163**, 461–486 (2011)
- K. Krohn, R. Jaumann, D. Elbeshausen, T. Kneissl, N. Schmedemann, J. Voigt, K. Otto, K.-D. Matz, F. Preusker, T. Roatsch, K. Stephan, R. Wagner, C.A. Raymond, C.T. Russell, Asymmetric craters on Vesta: impact on sloping surfaces. *Planet. Space Sci.* **103**, 36–56 (2014). <https://doi.org/10.1016/j.pss.2014.04.011>
- K. Krohn, I. von der Gathen, D.L. Buczkowski, R. Jaumann, K. Wickhusen, F. Schulzeck, K. Stephan, R. Wagner, J.C.E. Scully, C.A. Raymond, C.T. Russell, Fracture geometry and statistics of Ceres' floor fractures. *Planet. Space Sci.* **187**, 104955 (2020). <https://doi.org/10.1016/j.pss.2020.104955>
- Z.A. Landsman, J.P. Emery, H. Campins, J. Hanuš, L.F. Lim, D.P. Cruikshank, Asteroid (16) Psyche: evidence for a silicate regolith from spitzer space telescope spectroscopy. *Icarus* **304**, 58–73 (2018). <https://doi.org/10.1016/j.icarus.2017.11.035>

- D.S. Lauretta, D.N. DellaGiustina, C.A. Bennett et al., The unexpected surface of asteroid (101955) Bennu. *Nature* **568**, 55–60 (2019). <https://doi.org/10.1038/s41586-019-1033-6>
- L. Le Corre, V. Reddy, J. Sanchez, T. Dunn, E. Cloutis, M. Izawa, P. Mann, A. Nathues, Exploring exogenic sources for the olivine on Asteroid (4) Vesta. *Icarus* **258**, 483–499 (2015). <https://doi.org/10.1016/j.icarus.2015.01.018>
- J. Li, *Body-Fixed Coordinate Systems for Asteroid (4) Vesta, Planetary Data System* (2012)
- G. Libourel, A.M. Nakamura, P. Beck, S. Potin, C. Ganino, S. Jacomet et al., Hypervelocity impacts as a source of deceiving surface signatures on iron-rich asteroids. *Sci. Adv.* **5**(8), eaav3971 (2019). <https://doi.org/10.1126/sciadv.aav3971>
- R.M.C. Lopes, Io: the volcanic moon, in *Encyclopedia of the Solar System*, ed. by L.-A. McFadden, P.R. Weissman, T.V. Johnson 2nd edn. (Academic Press, San Diego, 2007), pp. 419–430. <https://doi.org/10.1016/B978-012088589-3/50026-8>. Chap. 22
- D.F. Lupishko, I.N. Belskaya, On the surface composition of the M-type asteroids. *Icarus* **78**, 395–401 (1989)
- X. Mao, W.B. McKinnon, Spin evolution of Ceres and Vesta due to impacts. *Meteorit. Planet. Sci.* **55**, 2493–2518 (2020). <https://doi.org/10.1111/maps.13594>
- S. Marchi, D.D. Durda, C.A. Polanskey, E. Asphaug, W.F. Bottke, L.T. Elkins-Tanton et al., Hypervelocity impact experiments in iron-nickel ingots and meteorites: implications for the NASA Psyche mission. *J. Geophys. Res., Planets* **125**(2), e2019JE005927 (2019). <https://doi.org/10.1029/2019JE005927>
- S. Marchi, D.D. Durda, C.A. Polanskey, E. Asphaug, W.F. Bottke, L.T. Elkins-Tanton et al., Hypervelocity impact experiments in iron-nickel ingots and iron meteorites: implications for the NASA Psyche mission. *J. Geophys. Res., Planets* **125**, e2019JE005927 (2020). <https://doi.org/10.1029/2019JE005927>
- S. Marchi, E. Asphaug, J. Bell, W.F. Bottke, R. Jaumann, R.S. Park, C.A. Polanskey, T. Prettyman, D.A. Williams, W.E. Page, Determining the relative ages of regions of Psyche's surface. *Space Sci. Rev.* (2022, this journal)
- M. Marsset, M. Brož, P. Vernazza et al., The violent collisional history of aqueously evolved (2) Pallas. *Nat. Astron.* **4**, 569–576 (2020). <https://doi.org/10.1038/s41550-019-1007-5>
- T. Matsumoto, D. Harries, F. Langenhorst et al., Iron whiskers on asteroid Itokawa indicate sulfide destruction by space weathering. *Nat. Commun.* **11**, 1117 (2020). <https://doi.org/10.1038/s41467-020-14758-3>
- A. Matter, M. Delbo, L.S. Carry, Evidence of a metal-rich surface for the Asteroid (16) Psyche from interferometric observations in the thermal infrared. *Icarus* **226**, 419–427 (2013). <https://doi.org/10.1016/j.icarus.2013.06.004>
- J-G. Moreau, T. Kohout, K. Wünnemann, P. Halodova, J. Haloda, Shock physics mesoscale modeling of shock stage 5 and 6 in ordinary and enstatite chondrites. *Icarus* **332**, 50–65 (2019). <https://doi.org/10.1016/j.icarus.2019.06.004>
- A. Neesemann, S. van Gasselt, S.H.G. Walter, R. Jaumann, J.C. Castillo-Rogez, C.A. Raymond, C.T. Russell, F. Postberg, Mapping of Ceres by Dawn: generation of higher level cartographic products based on Framing Camera Data, in *53rd Lunar and Planetary Science Conference*, March 7–11, 2022 (2022)
- G.A. Neumann, D.D. Rowlands, F.G. Lemoine, D.E. Smith, M.T. Zuber, Crossover analysis of Mars Orbiter Laser Altimeter data. *J. Geophys. Res.* **106**, 23,753–23,768 (2001). <https://doi.org/10.1029/2000JE001381>
- T. Noguchi, M. Kimura, T. Hashimoto, M. Konno, T. Nakamura, M.E. Zolensky, R. Okazaki, M. Tanaka, A. Tsuchiyama, A. Nakato, T. Ogami, H. Ishida, R. Sagae, S. Tsujimoto, T. Matsumoto, J. Matsuno, A. Fujimura, M. Abe, T. Yada, T. Mukai, M. Ueno, T. Okada, K. Shirai, Y. Ishibashi, Space weathered rims found on the surfaces of the Itokawa dust particles. *Meteorit. Planet. Sci.* **49**, 88–214 (2014)
- K.A. Otto, R. Jaumann, K. Krohn, K.-M. Matz, F. Preusker, T. Roatsch, P. Schenk, F. Scholten, K. Stephan, C.A. Raymond, C.T. Russell, Mass wasting features and processes in Vesta's south polar basin Rheasilvia. *J. Geophys. Res.* **118**, 2263–2437 (2013). <https://doi.org/10.1002/2013JE004333>
- K.A. Otto, R. Jaumann, K. Krohn, F. Spahn, C.A. Raymond, C.T. Russell, The Coriolis effect on mass wasting during the Rheasilvia impact on asteroid Vesta. *Geophys. Res. Lett.* **43**, 12340–12347 (2016). <https://doi.org/10.1002/2016GL071539>
- K.A. Otto, S. Marchi, A. Trowbridge, H.J. Melosh, H.G. Sizemore, Ceres Crater degradation inferred from concentric fracturing. *J. Geophys. Res., Planets* **124**, 1188–1203 (2019). <https://doi.org/10.1029/2018JE005660>
- D.W. Parcher, G.J. Whiffen, Dawn statistical maneuver design for Vesta operations, in *Paper AAS 2011-180, AIAA/AAS Astrodynamics Specialist Conference*, New Orleans, Louisiana, USA, Feb. 13–17, 2011 (2011)
- R.S. Park, A.S. Konopliv, B.G. Bills, N. Rambaux, J.C. Castillo-Rogez, C.A. Raymond, A.T. Vaughan, A.I. Ermakov, M.T. Zuber, R.R. Fu, M.J. Toplis, C.T. Russell, A. Nathues, F. Preusker, A partially differentiated interior for Ceres deduced from its gravity field and shape. *Nature* **537**, 515–517 (2016). <https://doi.org/10.1038/nature18955>

- R.S. Park, A.T. Vaughan, A.S. Konopliv, A.I. Ermakov, N. Mastrodemos, J.C. Castillo-Rogez, S.P. Joy, A. Nathues, C.A. Polansky, M.D. Rayman, J.E. Riedel, C.A. Raymond, C.T. Russell, M.T. Zuber, High-resolution shape model of Ceres from stereophotoclinometry using Dawn Imaging Data. *Icarus* **319**, 812–827 (2019). <https://doi.org/10.1016/j.icarus.2018.10.024>
- D.E. Pavlis et al., GEODYN operations manuals. Raytheon ITTS Contractor Report, Lanham, MD (2001)
- C.M. Pieters, L.A. Taylor, S.K. Noble, L.P. Keller, B. Hapke, R.V. Morris, C.C. Allen, D.S. McKay, S. Wentworth, Space weathering on airless bodies: resolving a mystery with lunar samples. *Meteorit. Planet. Sci.* **35**, 1101–1107 (2000)
- C. Pieters, E. Ammann, D. Blewett et al., Distinctive space weathering on Vesta from regolith mixing processes. *Nature* **491**, 79–82 (2012). <https://doi.org/10.1038/nature11534>
- J.B. Plescia, M.P. Golombek, Origin of planetary wrinkle ridges based on the study of terrestrial analogs. *Geol. Soc. Am. Bull.* **97**, 1289–1299 (1986)
- C.A. Polansky, S.P. Joy, C.A. Raymond, Efficacy of the Dawn Vesta science plan, in *12th International Conference on Space Operations 2012*, Stockholm, Sweden, June 2012 (2012)
- C.A. Polansky, L. Elkins-Tanton, R. Jaumann, D.J. Lawrence, D.M. Marsh, R.R. Moore et al., Psyche science operations concept: maximize reuse to minimize risk, in *2018 SpaceOps Conference* (2018), p. 2703
- C.A. Polansky et al., *Space Sci. Rev.* (2022, this journal)
- F. Preusker, F. Scholten, J. Knollenberg, E. Kührt, K.-D. Matz, S. Mottola, T. Roatsch, N. Thomas, The northern hemisphere of asteroid (21) Lutetia – topography and orthoimages from Rosetta OSIRIS NAC image data. *Planet. Space Sci.* **66**, 54–63 (2012)
- F. Preusker, F. Scholten, K.-D. Matz et al., Shape model, reference system definition, and cartographic mapping standards for comet 67P/Churyumov-Gerasimenko – stereo-photogrammetric analysis of Rosetta/OSIRIS image data. *Astron. Astrophys.* **583**, A33 (2015). <https://doi.org/10.1051/0004-6361/201526349>
- F. Preusker, F. Scholten, K.D. Matz, S. Elgner, R. Jaumann, T. Roatsch, S.P. Joy, C.A. Polansky, C.A. Raymond, C.T. Russell, Dawn at Ceres – shape model and rotational state, in *47th Lunar and Planetary Science Conference [#1954]*, March 21–25, 2016 (2016)
- F. Preusker, F. Scholten, S. Elgner, K.-D. Matz, R.T. Kameda, R. Jaumann, S. Sugita, S. Honda, T. Morota, E. Tatsumi, Y. Cho, K. Yoshioka, S. Sawada, Y. Yokota, N. Sakatani, M. Hayakawa, M. Matsuoka, M. Yamada, T. Kouyama, H. Suzuki, C. Honda, K. Ogawa, The MASCOT landing area on asteroid (162173) Ryugu: stereo-photogrammetric analysis using images of the ONC onboard the Hayabusa2 spacecraft. *Astron. Astrophys.* **632**, L4 (2019). <https://doi.org/10.1051/00046361/201936759>
- M.D. Rayman, R.A. Mase, Dawn’s exploration of Vesta. *Acta Astronaut.* **94**, 159–167 (2014)
- C.A. Raymond, R. Jaumann, A. Nathues, H. Sierks, T. Roatsch, F. Preusker, F. Scholten, R.W. Gaskell, L. Jorda, H.-U. Keller, M.T. Zuber, D.E. Smith, N. Mastrodemos, S. Mottola, The Dawn topography investigation. *Space Sci. Rev.* **163**, 487–510 (2011). <https://doi.org/10.1007/s11214-011-9863-z>
- T. Roatsch, E. Kersten, K.-M. Matz, F. Preusker, F. Scholten, R. Jaumann, C.A. Raymond, C.T. Russell, High resolution Vesta High Altitude Mapping Orbit (HAMO) Atlas derived from Dawn framing camera images. *Planet. Space Sci.* **73**, 283–286 (2012). <https://doi.org/10.1016/j.pss.2012.08.021>
- T. Roatsch, E. Kersten, A. Hoffmeister, M. Wählisch, K.-D. Matz, C.C. Porco, Recent improvements of the Saturnian satellite atlases: Mimas, Enceladus, and Dione. *Planet. Space Sci.* **77**, 118–125 (2013). <https://doi.org/10.1016/j.pss.2012.02.016>
- T. Roatsch, E. Kersten, K.-D. Matz, F. Preusker, F. Scholten, R. Jaumann, C.A. Raymond, C.T. Russell, Ceres Survey Atlas derived from Dawn Framing Camera images. *Planet. Space Sci.* **121**, 115–120 (2016). <https://doi.org/10.1016/j.pss.2015.12.005>
- D.D. Rowlands et al., GEODYN II system description. Hughes-STX Contractor Report, Greenbelt, MD (1993)
- C.T. Russell, H.Y. McSween, R. Jaumann, C.A. Raymond, The Dawn mission to Vesta and Ceres, in *Asteroids IV*, ed. by P. Michel, F.E. DeMeo, W.F. Bottke (Univ. of Arizona Press, Tucson, 2015), pp. 419–433
- S. Sasaki, K. Nakamura, Y. Hamabe, E. Kurahashi, T. Hiroi, Production of iron nanoparticles by laser irradiation in a simulation of lunar-like space weathering. *Nature* **410**, 555–557 (2001)
- P. Schenk, D.P. O’Brien, S. Marchi, R. Gaskell, F. Preusker, T. Roatsch, R. Jaumann, D. Buczkowski, T. McCord, H.Y. McSween, D. Williams, A. Yingst, R. Raymond, C. Russell, The geologically recent giant impact basins at Vesta’s south pole. *Science* **336**, 694–697 (2012). <https://www.science.org/doi/full/10.1126/science.1223272>
- P. Schenk, J. Castillo-Rogez, K.A. Otto, S. Marchi, D. O’Brien, H.K. Bland, B. Schmidt, J. Scully, D. Buczkowski, K. Krohn, T. Hoogenboom, G. Kramer, V. Bray, A. Neesemann, H. Hiesinger, T. Platz, M.C. De Sanctis, S. Schroeder, L. Le Corre, L. McFadden, M. Sykes, C. Raymond, C.T. Russell, Compositional control on impact crater formation on mid-sized planetary bodies: Dawn at Ceres and Vesta, Cassini at Saturn. *Icarus* **359**, 114343 (2021). <https://doi.org/10.1016/j.icarus.2021.114343>

- N. Schmedemann, T. Kneissl, B.A. Ivanov, G.G. Michael, R.J. Wagner, G. Neukum, O. Ruesch, H. Hiesinger, K. Krohn, P.F. Roatsch, H. Sierks, R. Jaumann, V. Reddy, A. Natheus, S.H.G. Walter, A. Neesemann, C.A. Raymond, C.T. Russell, The cratering record, chronology, and surface ages of (4) Vesta in comparison to smaller asteroids and the ages of HED meteorites. *Planet. Space Sci.* **103**, 104–130 (2014). <https://doi.org/10.1016/j.pss.2014.04.004>
- F. Scholten, K. Gwinner, T. Roatsch, K.-D. Matz, M. Wählisch, B. Giese, J. Oberst, R. Jaumann, G. Neukum (HRSC Co-Investigator Team), Mars Express HRSC data processing – methods and operational aspects. *Photogramm. Eng. Remote Sens.* **71**(10), 1143–1152 (2005)
- F. Scholten, J. Oberst, K.-D. Matz, T. Roatsch, M. Wählisch, M.S. Robinson (the LROC Team), Towards global lunar topography using LROC WAC stereo data, in *41st Lunar and Planetary Science Conference*, #2111 (2009)
- F. Scholten, F. Preusker, S. Elgner, K.-D. Matz, R. Jaumann, M. Hamm, S.E. Schroeder, A. Koncz, N. Schmitz, F. Trauthan, M. Grott, J. Biele, T.-M. Ho, S. Kameda, S. Sugita, The Hayabusa2 lander MAS-COT on the surface of asteroid (162173) Ryugu – stereo-photogrammetric analysis of MASCam image data. *Astron. Astrophys.* **632**, L5 (2019). <https://doi.org/10.1051/0004-6361/201936760>
- S.E. Schroeder, S. Mottola, H.U. Keller, C.A. Raymond, C.T. Russell, Resolved photometry of Vesta reveals physical properties of crater regolith. *Planet. Space Sci.* **85**, 198–213 (2013). <https://doi.org/10.1016/j.pss.2013.06.009>. ISSN 0032-0633
- M. Shepard, J. Richardson, P.A. Taylor, L.A. Rodrigues-Ford, A. Conrad, I. de Pater, M. Adamkovic, K. de Kleer, J.R. Males, K.M. Morzinski, L.M. Close, M. Kaasalainen, M. Viikinkoski, B. Timerson, V. Reddy, C. Magri, M.C. Nolan, E.S. Howell, L.A.M. Benner, J.D. Giorgini, B.D. Warner, A.W. Harris, Radar observations and shape model of asteroid 16 Psyche. *Icarus* **281**, 388–403 (2017). <https://doi.org/10.1016/j.icarus.2016.08.011>
- L. Siltala, M. Granvik, Mass and density of asteroid (16) Psyche. *ApJL* (2021, in press). [2103.01707v1](https://arxiv.org/abs/2103.01707v1) [astro-ph.EP]
- J.A. Skinner, A.E. Huff Jr., C.M. Fortezzo, T.A. Giather, T.M. Hare, M.A. Hunter, Planetary Geologic Mapping Protocol – 2018 (2018). Downloadable at: https://astropedia.astrogeology.usgs.gov/download/Docs/Mappers/PGM_Protocol_March_2018.pdf
- K. Stephan, R. Jaumann, M.C. De Sanctis, F. Tosi, E. Ammannito, K. Krohn, F. Zambon, S. Marchi, O. Ruesch, K.D. Matz, F. Preusker, T. Roatsch, C.A. Raymond, C.T. Russell, Small fresh impact craters on asteroid 4 Vesta: a compositional and geological fingerprint. *J. Geophys. Res., Planets* **119**(4), 2013JE004388 (2014)
- S. Sugita, R. Honda, T. Morota, S. Kameda, H. Sawada, E. Tatsumi, M. Yamada, C. Honda, Y. Yokota, T. Kouyama, N. Sakatani, K. Ogawa, H. Suzuki, T. Okada, N. Namiki, S. Tanaka, Y. Iijima, K. Yoshioka, M. Hayakawa, Y. Cho, M. Matsuoka, N. Hirata, H. Miyamoto, D. Domingue, M. Hirabayashi, T. Nakamura, T. Hiroi, T. Michikami, P. Michel, R.-L. Ballouz, O.S. Barnouin, C.M. Ernst, S.E. Schröder, H. Kikuchi, R. Hemmi, G. Komatsu, T. Fukuhara, M. Taguchi, T. Arai, H. Senshu, H. Demura, Y. Ogawa, Y. Shimaki, T. Sekiguchi, T.G. Müller, A. Hagermann, T. Mizuno, H. Noda, K. Matsumoto, R. Yamada, Y. Ishihara, H. Ikeda, H. Araki, K. Yamamoto, S. Abe, F. Yoshida, A. Higuchi, S. Sasaki, S. Oshigami, S. Tsuruta, K. Asari, S. Tazawa, M. Shizugami, J. Kimura, T. Otsubo, H. Yabuta, S. Hasegawa, M. Ishiguro, S. Tachibana, E. Palmer, R. Gaskell, L. Le Corre, R. Jaumann, K. Otto, N. Schmitz, P.A. Abell, M.A. Barucci, M.E. Zolensky, F. Vilas, F. Thuillet, C. Sugimoto, N. Takaki, Y. Suzuki, H. Kamiyoshihara, M. Okada, K. Nagata, M. Fujimoto, M. Yoshikawa, Y. Yamamoto, K. Shirai, R. Noguchi, N. Ogawa, F. Terui, S. Kikuchi, T. Yamaguchi, Y. Oki, Y. Takao, H. Takeuchi, G. Ono, Y. Mimasu, K. Yoshikawa, T. Takahashi, Y. Takei, A. Fujii, C. Hirose, S. Nakazawa, S. Hosoda, O. Mori, T. Shimada, S. Soldini, T. Iwata, M. Abe, H. Yano, R. Tsukizaki, M. Ozaki, K. Nishiyama, T. Saiki, S. Watanabe, Y. Tsuda, The geomorphology, color, and thermal properties of Ryugu: implications for parent-body processes. *Science* **364**, 252 (2019)
- M. Tenthoff, K. Wohlfarth, C. Wöhler, High resolution digital terrain models of Mercury. *Remote Sens.* **12**(23), 3989 (2020). <https://doi.org/10.3390/rs12233989>
- P.C. Thomas, R.R. Benz, M.J. Gaffey, B.H. Zellner, A.D. Storrs, E. Wells, Vesta: spin pole, size, and shape from HST images. *Icarus* **128**, 88–94 (1997)
- P.C. Thomas, J. Joseph, B. Carcich, J. Veverka, B.E. Clark, J.F. Bell, A.W. Byrd, R. Chomko, M. Robinson, S. Murchie, L. Prockter, A. Cheng, N. Izenberg, M. Malin, C. Chapman, L.A. McFadden, R. Kirk, M. Gaffey, P.G. Lucey, Eros: shape, topography, and slope processes. *Icarus* **155**(1), 18–37 (2002). <https://doi.org/10.1006/icar.2001.6755>
- M. Viikinkoski, P. Vernazza, J. Hanuš, H. Le Corroller, K. Tazhenova et al., (16) Psyche: a mesosiderite-like asteroid? *Astron. Astrophys.* **619**, 619 (2018). <https://doi.org/10.1051/0004-6361/201834091>
- S. Watanabe, M. Hirabayashi, N. Hirata, N. Hirata, R. Noguchi, Y. Shimaki, H. Ikeda, E. Tatsumi, M. Yoshikawa, S. Kikuchi, H. Yabuta, T. Nakamura, S. Tachibana, Y. Ishihara, T. Morota, K. Kitazato, N. Sakatani, K. Matsumoto, K. Wada, H. Senshu, C. Honda, T. Michikami, H. Takeuchi, T. Kouyama, R.

- Honda, S. Kameda, T. Fuse, H. Miyamoto, G. Komatsu, S. Sugita, T. Okada, N. Namiki, M. Arakawa, M. Ishiguro, M. Abe, R. Gaskell, E. Palmer, O.S. Barnouin, P. Michel, A.S. French, J.W. McMahon, D.J. Scheeres, P.A. Abell, Y. Yamamoto, S. Tanaka, K. Shirai, M. Matsuoka, M. Yamada, Y. Yokota, H. Suzuki, K. Yoshioka, Y. Cho, N. Nishikawa, T. Sugiyama, H. Kikuchi, R. Hemmi, T. Yamaguchi, N. Ogawa, G. Ono, Y. Mimasu, K. Yoshikawa, T. Takahashi, Y. Takei, A. Fujii, C. Hirose, T. Iwata, M. Hayakawa, S. Hosoda, O. Mori, H. Sawada, T. Shimada, S. Soldini, H. Yano, R. Tsukizaki, M. Ozaki, Y. Iijima, K. Ogawa, M. Fujimoto, T.-M. Ho, A. Moussi, R. Jaumann, J.-P. Bibring, C. Krause, F. Terui, T. Saiki, S. Nakazawa, Y. Tsuda, Hayabusa2 arrives at the carbonaceous asteroid 162173 Ryugu – a spinning top-shaped rubble pile. *Science* **364**, 268–272 (2019)
- T.R. Watters, A case for limited global contraction of Mercury. *Commun. Earth Environ.* **2**, 9 (2021). <https://doi.org/10.1038/s43247-020-00076-5>
- D.A. Williams, R. Jaumann, H.Y. McSween Jr., C.A. Raymond, S. Marchi, N. Schmedemann, C.T. Russell, The chronostratigraphy of protoplanet Vesta. *Icarus* **244**, 158–165 (2014). <https://doi.org/10.1016/j.icarus.2014.06.027>
- M.T. Zuber, D.E. Smith, A.F. Cheng, J.B. Garvin, O. Aharonson, T.D. Cole, P.J. Dunn, Y. Guo, F.G. Lemoine, G.A. Neumann, D.D. Rowlands, M.H. Torrence, The shape of 433 Eros from the NEAR-shoemaker laser rangefinder. *Science* **289**, 2097–2101 (2000). <https://doi.org/10.1126/science.289.5487.2097>
- M.T. Zuber, R.S. Park, L.T. Elkins-Tanton, J. Bell, K.N. Bruvold, D. Bercovici, B.R. Bills, R.P. Binzel, R. Jaumann, S. Marchi, C.A. Polanski, C.A. Raymond, T. Roatsch, C. Wang, B.P. Weiss, M.A. Wieczorek, The Psyche gravity investigation. *Space Sci. Rev.* (2022, this journal)

Publisher's Note Springer Nature remains neutral with regard to jurisdictional claims in published maps and institutional affiliations.

Authors and Affiliations

Ralf Jaumann¹  · James F. Bell III² · Carol A. Polanskey³ · Carol A. Raymond³ · Erik Aspaugh⁴ · David Bercovici⁵ · Bruce R. Bills³ · Richard Binzel⁶ · William Bottke⁷ · John M. Christoph² · Simone Marchi⁷ · Alicia Neesemann¹ · Katharina Otto⁸ · Ryan S. Park³ · Frank Preusker⁸ · Thomas Roatsch⁸ · David A. Williams² · Mark A. Wieczorek⁹ · Maria T. Zuber⁶

✉ R. Jaumann
ralf.jaumann@fu-berlin.de

¹ Freie Universitaet Berlin, Institute of Geological Sciences, 12249 Berlin, Germany

² School of Earth and Space Exploration, Arizona State University, Tempe, AZ 86387-2001, USA

³ Jet Propulsion Laboratory, Pasadena, CA 91109, USA

⁴ Lunar and Planetary Laboratory, Tucson, AZ, USA

⁵ Department of Earth and Planetary Sciences, Yale University, New Haven, CT 06520, USA

⁶ Department of Earth, Atmospheric, and Planetary Sciences, Massachusetts Institute of Technology, Cambridge, MA 02139, USA

⁷ Southwest Research Institute, Boulder, CO 80302, USA

⁸ Deutsches Zentrum für Luft- und Raumfahrt, Institute of Planetary Research, Berlin, Germany

⁹ Université Côte d'Azur, Observatoire de la Côte d'Azur CNRS, Laboratoire Lagrange, Nice, France